

Mountain wave turbulence in the presence of directional wind shear over the Rocky Mountains

Article

Accepted Version

Guarino, M. V., Teixeira, M. A. C. ORCID: <https://orcid.org/0000-0003-1205-3233>, Keller, T. L. and Sharman, R. D. (2018) Mountain wave turbulence in the presence of directional wind shear over the Rocky Mountains. *Journal of the Atmospheric Sciences*, 75 (4). pp. 1285-1305. ISSN 1520-0469 doi: 10.1175/JAS-D-17-0128.1 Available at <https://centaur.reading.ac.uk/75677/>

It is advisable to refer to the publisher's version if you intend to cite from the work. See [Guidance on citing](#).

Published version at: <https://journals.ametsoc.org/doi/10.1175/JAS-D-17-0128.1>

To link to this article DOI: <http://dx.doi.org/10.1175/JAS-D-17-0128.1>

Publisher: American Meteorological Society

All outputs in CentAUR are protected by Intellectual Property Rights law, including copyright law. Copyright and IPR is retained by the creators or other copyright holders. Terms and conditions for use of this material are defined in the [End User Agreement](#).

www.reading.ac.uk/centaur

CentAUR

Central Archive at the University of Reading

Reading's research outputs online



AMERICAN METEOROLOGICAL SOCIETY

Journal of the Atmospheric Sciences

EARLY ONLINE RELEASE

This is a preliminary PDF of the author-produced manuscript that has been peer-reviewed and accepted for publication. Since it is being posted so soon after acceptance, it has not yet been copyedited, formatted, or processed by AMS Publications. This preliminary version of the manuscript may be downloaded, distributed, and cited, but please be aware that there will be visual differences and possibly some content differences between this version and the final published version.

The DOI for this manuscript is doi: 10.1175/JAS-D-17-0128.1

The final published version of this manuscript will replace the preliminary version at the above DOI once it is available.

If you would like to cite this EOR in a separate work, please use the following full citation:

Guarino, M., M. Teixeira, T. Keller, and R. Sharman, 2018: Mountain wave turbulence in the presence of directional wind shear over the Rocky Mountains. *J. Atmos. Sci.* doi:10.1175/JAS-D-17-0128.1, in press.

© 2018 American Meteorological Society



1 **Mountain wave turbulence in the presence of directional wind shear over**
2 **the Rocky Mountains**

3 Maria-Vittoria Guarino*, Miguel A. C. Teixeira

4 *Department of Meteorology, University of Reading, UK*

5 Teddie L. Keller, Robert D. Sharman

6 *National Center for Atmospheric Research, Boulder, Colorado*

7 * *Corresponding author address: Present address: Maria Vittoria Guarino, British Antarctic Survey,*

8 *High Cross, Madingley Road, Cambridge CB3 0ET, UK.*

9 *E-mail: m.v.guarino@bas.ac.uk*

ABSTRACT

10 Mountain wave turbulence in the presence of directional wind shear over
11 the Rocky Mountains in Colorado is investigated. Pilot Reports (PIREPs)
12 are used to select cases in which moderate or severe turbulence encounters
13 were reported in combination with significant directional wind shear in the
14 upstream sounding from Grand Junction, CO (GJT). For a selected case,
15 semi-idealized numerical simulations are carried out using the WRF-ARW
16 atmospheric model, initialized with the GJT atmospheric sounding and a re-
17 alistic but truncated orography profile. In order to isolate the role of direc-
18 tional wind shear in causing wave breaking, sensitivity tests are performed
19 to exclude the variation of the atmospheric stability with height, the speed
20 shear, and the mountain amplitude as dominant wave breaking mechanisms.
21 Significant downwind transport of instabilities is detected in horizontal flow
22 cross-sections, resulting in mountain-wave-induced turbulence occurring at
23 large horizontal distances from the first wave breaking point (and from the
24 orography that generates the waves). The existence of an *asymptotic wake*, as
25 predicted by Shutts for directional shear flows, is hypothesized to be respon-
26 sible for this downwind transport. Critical levels induced by directional wind
27 shear are further studied by taking 2D power spectra of the magnitude of the
28 horizontal velocity perturbation field. In these spectra, a rotation of the most
29 energetic wave modes with the background wind, as well as perpendicular-
30 ity between the background wind vector and the wave-number vector of those
31 modes at critical levels, can be found, which is consistent with the mechanism
32 expected to lead to wave breaking in directional shear flows.

33 **1. Introduction**

34 Mountain waves, also known as orographic gravity waves, result from stably stratified airflow
35 over orography. These waves can break at different altitudes and influence the atmosphere both
36 locally, by generating, for example, aviation-scale turbulence (Lilly 1978), and globally, by de-
37 celerating the general atmospheric circulation (Lilly and Kennedy 1973). Several studies have
38 investigated the role of mountain wave activity in a wide range of atmospheric processes taking
39 place in the boundary layer (e.g. Durran (1990), Grubišić et al. (2015)), in the mid-troposphere
40 (e.g. Jiang and Doyle (2004), Strauss et al. (2015)), in the upper-troposphere (e.g. Worthington
41 (1998), Whiteway et al. (2003), McHugh and Sharman (2013)), in the stratosphere (e.g. Carslaw
42 et al. (1998), Eckermann et al. (2006)), and in the mesosphere (e.g. Broutman et al. (2017)).

43 Orographic gravity wave breaking in the mid- and upper-troposphere can generate turbulence at
44 aircraft-cruising altitudes. This is one of the known forms of Clear-Air Turbulence (CAT), and it
45 occurs, among other occasions, when large amplitude waves approach critical levels, as this leads
46 to a further increase of the wave amplitude. Critical levels correspond to singularities in the wave
47 equation, where waves cease to propagate and break or are absorbed into the mean flow (Dörnbrack
48 et al. (1995), Grubišić and Smolarkiewicz (1997)), and above which the wave motion is no longer
49 sustained, provided the Richardson number of the background flow is larger than about 1 (Booker
50 and Bretherton 1967). For atmospheric flows where the wind direction changes with height, the
51 existence of critical levels is controlled by the relative orientations of the background wind vector
52 and the horizontal wave-number vector at each height. Broad (1995) and Shutts (1995) used linear
53 theory to investigate the effects of directional wind shear on the gravity wave momentum fluxes,
54 introducing the theoretical and mathematical framework for gravity wave drag in winds that turn
55 with height.

56 Generally, mountain wave critical levels exist when $\mathbf{U} \cdot \boldsymbol{\kappa}_H = u_0 k + v_0 l = 0$ (where $\mathbf{U} \equiv (u_0, v_0)$
57 is the background wind velocity and $\boldsymbol{\kappa}_H \equiv (k, l)$ is the horizontal wave-number vector) (Teixeira
58 2014). For unidirectional shear flows ($u_0 = f(z)$, $v_0 = 0$, where f is an arbitrary function) or
59 flows over two-dimensional ridges ($l = 0$), the definition of critical level reduces to $u_0 = 0$. For
60 directional shear flows ($u_0 = f(z)$, $v_0 = g(z)$, where f and g are arbitrary functions) over idealized
61 three-dimensional or complex (i.e. realistic) orographies (where $k \neq 0$, $l \neq 0$), critical levels occur
62 when the wind vector is perpendicular to the horizontal wave-number vector, as expressed by the
63 general condition presented above. This condition is difficult to assess from standard physical
64 data, as the orientations of the wave-number vectors can only be evaluated in Fourier space.

65 Previous theoretical and numerical studies investigating mountain waves in directional shear
66 flows include Shutts (1998) and Shutts and Gadian (1999), who studied the structure of the moun-
67 tain wave field in the presence of directional wind shear; Teixeira et al. (2008), Teixeira and Mi-
68 randa (2009) and Xu et al. (2012), who focused on the impact of directional wind shear on the
69 mountain wave momentum flux and, thus, on the gravity wave drag exerted on the atmosphere;
70 and Guarino et al. (2016), who investigated the conditions for mountain wave breaking in direc-
71 tional shear flows and their implications for CAT generation. All these studies considered idealized
72 situations with a wind direction that turns continuously with height. This flow configuration is the
73 simplest possible with directional wind shear, and represents a prototype of more realistic flows.

74 We are aware of only two observational studies of this problem in the literature focused on real
75 cases: Doyle and Jiang (2006) studied a wave breaking event in the presence of directional wind
76 shear observed over the French Alps during the Mesoscale Alpine Programme (MAP), whereas
77 Lane et al. (2009) studied aircraft turbulence encounters over Greenland, and attributed the ob-
78 served generation of flow instabilities to the interaction between mountain waves and directional
79 critical levels.

80 In this paper, mountain wave turbulence occurring in the presence of directional wind shear over
81 the Rocky Mountains in Colorado is investigated. Numerical simulations for a selected turbulence
82 encounter are performed using a semi-idealized approach, for which the WRF-ARW atmospheric
83 model is used in an idealized configuration, but initialized with the real (albeit truncated) orog-
84 raphy and a realistic atmospheric profile. A similar mixed approach, consisting of simulating
85 a real event using a rather idealized model configuration, has been used in the past, for exam-
86 ple, by Doyle et al. (2000), to study the 11 January 1972 Boulder windstorm and by Kirshbaum
87 et al. (2007), to study orographic rain-bands triggered by lee waves over the Oregon coastal range.
88 This method allows us to retain the elements necessary to reproduce the mechanisms responsible
89 for mountain wave generation and breaking, while working in simplified conditions that facili-
90 tate physical interpretation. The simulation results are compared with theory and with idealized
91 simulations, for a more comprehensive description and better physical understanding of the flow.
92 The aim is to isolate the role of directional wind shear and determine its relevance in causing the
93 observed turbulence event.

94 Because of its complexity, the wave breaking mechanism in directional shear flows is not cur-
95 rently taken into account for CAT forecasting purposes. Investigating its role in real turbulence
96 encounters, as this paper aims to do, is part of the fundamental research needed to improve the
97 forecasting methods of mountain wave turbulence, which is currently one of the most poorly pre-
98 dicted forms of CAT (Gill and Stirling 2013). In fact, although mountain wave turbulence is
99 included in the forecasts provided by the London World Area Forecast Centre (WAFC), its predic-
100 tion is still based on a method developed by Turner (1999), relying on diagnostics of the gravity
101 wave drag from its parametrization in a global model (which itself does not accurately represent
102 mountain wave absorption by directional wind shear). A first attempt to account for mountain
103 waves explicitly in CAT forecast was recently reported by Elvidge et al. (2017). The turbulence

104 forecasting system GTG, described in Sharman and Pearson (2016) also contains several explicit
 105 MWT algorithms, but none consider the effect of directional wind shear. Furthermore, a predictor
 106 for mountain wave CAT is absent in the forecast issued by the Washington WAFC (Gill 2014).

107 The remainder of the paper is organized as follows. In section 2, the mechanism leading to wave
 108 breaking in directional shear flows is discussed. In section 3, the methodology used to select the
 109 turbulence encounter investigated here and the set-up of the numerical simulations is presented. In
 110 section 4, the simulation results are described, and further discussed in the light of the sensitivity
 111 tests presented in the same section. In section 5, the main conclusions of the present study are
 112 summarized.

113 2. Wave breaking mechanism in directional shear flows

114 For a hydrostatic, adiabatic, three-dimensional and frictionless flow without Earth's rotation,
 115 under the Boussinesq approximation, the wave equation from linear theory (also known as Taylor-
 116 Goldstein equation) takes the form (Nappo 2012):

$$\widehat{w}'' + \left[\frac{(k^2 + l^2)N_0^2}{(ku_0 + lv_0)^2} - \frac{ku_0'' + lv_0''}{ku_0 + lv_0} \right] \widehat{w} = 0, \quad (1)$$

117 where \widehat{w} is the Fourier transform of the vertical velocity, N_0 is the Brunt-Väisälä frequency of the
 118 background flow, and the primes denote differentiation with respect to z .

119 In vertically sheared background flows, the solution to (1) can be approximated as (Teixeira et al.
 120 2004):

$$\widehat{w}(k, l, z) = \widehat{w}(k, l, 0) \left| \frac{m(z=0)}{m(z)} \right|^{1/2} e^{i \int_0^z m(z) dz}, \quad (2)$$

121 where the bottom boundary condition is $\widehat{w}(k, l, 0) = i(ku_0 + lv_0)\widehat{h}(k, l)$, and $\widehat{h}(k, l)$ is the Fourier
 122 transform of the terrain elevation $h(x, y)$. This corresponds to a first-order WKB approximation,

123 where the vertical wave-number m is defined as:

$$m = \frac{N_0(k^2 + l^2)^{1/2}}{(ku_0 + lv_0)} \quad (3)$$

124 as if N_0 , u_0 and v_0 were constant, but where these quantities depend on z . Equations (2)-(3) are
 125 valid for any wave-number vector (k, l) in the wave spectrum, as long as the background state
 126 variables N_0 and (u_0, v_0) vary sufficiently slowly with height. In addition, by mass conservation, it
 127 can be shown that the Fourier transforms of the horizontal velocity perturbations \hat{u}' and \hat{v}' are

$$\hat{u}'(k, l, z) = \hat{u}'(k, l, 0) \text{sign} \left(\frac{m(z)}{m(0)} \right) \left| \frac{m(z)}{m(0)} \right|^{1/2} e^{i \int_0^z m(z) dz}, \quad (4)$$

$$\hat{v}'(k, l, z) = \hat{v}'(k, l, 0) \text{sign} \left(\frac{m(z)}{m(0)} \right) \left| \frac{m(z)}{m(0)} \right|^{1/2} e^{i \int_0^z m(z) dz}. \quad (5)$$

128 Orographic gravity waves excited by an isolated or complex orography can always be repre-
 129 sented by a spectrum of wave-numbers, whose direction and amplitude depend on the bottom
 130 boundary condition (as shown by (2)). Hence, the wave equation has to be solved for each wave-
 131 number and, in physical space, the resulting wave pattern will be given by the Fourier integral (or
 132 sum) of their contributions (Nappo 2012).

133 From the equations shown above it can be seen that, in directional shear flows, the mountain
 134 wave equation (1) becomes singular at critical levels, where $\kappa_H \cdot \mathbf{U} = ku_0 + lv_0 = 0$. For a
 135 wave-number approaching its critical level, m approaches infinity according to (3), and the
 136 Fourier transform of the vertical velocity \hat{w} becomes small ($\hat{w} \rightarrow 0$) according to (2). On the other
 137 hand, according to (4)-(5), the Fourier transform of the horizontal velocity perturbation diverges
 138 ($(\hat{u}', \hat{v}') \rightarrow \infty$) (Shutts 1998). The net result is an increase of the wave amplitude in the vicinity of
 139 a critical level. However, only wave-numbers with large spectral amplitudes approaching critical
 140 levels will in practice contribute to wave breaking (since this process is intrinsically defined in
 141 physical space) and the subsequent generation of turbulence; small amplitude wave-numbers will

142 be absorbed at the critical levels, as described by linear theory (Booker and Bretherton 1967).
143 Note also that the products of \hat{u}' and \hat{w} , and of \hat{v}' and \hat{w} , remain finite near critical levels (as shown
144 by (2),(4)-(5), despite the divergence of \hat{u}' and \hat{v}' , since their amplification cancels out with the
145 attenuation of \hat{w} . These products would in fact be exactly constant with height if there were no
146 singularities in the integrals in the exponents of (2) and (4)-(5), which account for the absorbing
147 effect of critical levels (cf. Broad (1995), Teixeira and Miranda (2009)).

148

149 The diagnosis of critical levels induced by directional wind shear can only be made in Fourier
150 space (where the orientation and the amplitude of each wave-number may be determined), as
151 explained above, but it is the wave energy distribution by wave-number in the wave spectrum that
152 ultimately determines whether wave breaking occurs or not.

153 **3. Methodology**

154 *a. PIREPs and case study selection*

155 Pilot Reports (PIREPs) of turbulence were used to select cases where atmospheric turbulence
156 was reported, in the presence of directional wind shear, over the Rocky Mountains. An accurate
157 description of the PIREPs database used here is provided by Wolff and Sharman (2008). In the
158 same paper, those authors discuss generic issues and limitations of using pilot reports as a research
159 tool (see also Schwartz (1996)). Here, we recall that while PIREPs represent a reliable method to
160 determine turbulence occurrence, the information they provide about time, location and turbulence
161 intensity may not be accurate. More specifically, Sharman et al. (2006) showed that, on average,
162 the uncertainty associated with pilot reports is 50 km along the horizontal direction, 200 s in
163 time, and 70 m along the vertical direction. Despite this uncertainty, pilot reports have been

164 conveniently employed in studies aimed at evaluating/validating turbulence occurrence (Kim and
165 Chun (2010), Trier et al. (2012), Ágústsson and Ólafsson (2014), Keller et al. (2015)) for lack of
166 a better alternative.

167 In this paper, PIREPs are used to identify days where generic atmospheric turbulence, or moun-
168 tain wave turbulence (MWT), was reported by pilots over the Rocky Mountains in the state of
169 Colorado. In particular, moderate or severe turbulence reports within the upper troposphere (4
170 km to the tropopause height) are considered. The lowest 4 km of the atmosphere were excluded
171 to eliminate low-level turbulence and directional wind shear associated with boundary layer pro-
172 cesses. Note that the highest mountain peak considered here has about 4 km elevation (above sea
173 level), and the boundary layer height over mountainous terrain is expected to adjust to the terrain
174 elevation following the topography, so exclusion of the lowest 4 km should avoid the boundary
175 layer almost completely (DeWekker and Kossmann 2015).

176 The analysis focused on the winter seasons of two years of data: 2015 and 2016. Climatolo-
177 gies of mountain wave activity (Julian and Julian (1969), Wolff and Sharman (2008)) show that
178 this activity is larger over the Rocky Mountains during the winter months, when low-level winds
179 are strong and westerly (i.e. perpendicular to the dominant mountain ridges). Furthermore, the
180 stronger jet stream in winter favours the existence of both speed and directional wind shear via
181 the thermal wind relation. The atmospheric conditions were evaluated using soundings mea-
182 sured upstream of the Rocky Mountains. The meteorological station selected was Grand Junc-
183 tion (Fig. 1), and the data were downloaded from the website of the University of Wyoming
184 (<http://weather.uwyo.edu/upperair/sounding.html>). In Fig. 2 the wind speed and direction, as
185 well as the atmospheric stability (quantified through the squared Brunt-Väisälä frequency N^2) are
186 shown for 7th February 2015 at 00 UTC. This day was chosen as a case study because of the fairly
187 continuous change of wind direction with height and a tropopause height of about 11 km. The

188 existence of a high tropopause facilitates excluding the stability change with height taking place
189 in its vicinity from the possible mechanisms causing wave breaking and, thus, responsible for the
190 turbulence encounters reported in the first 10 km of the atmosphere (further indications that this
191 is plausible are given below). As can be seen in Fig. 2, the rate of wind turning with height is
192 not constant, but varies from a maximum of 50 degrees km^{-1} at lower levels (up to 4 km) and 10
193 degrees km^{-1} at higher altitudes (6 - 8 km), to a slower rotation rate (between 3 degrees km^{-1} and
194 5 degrees km^{-1}) in the atmospheric layers between 4 and 6 km and above 10 km, respectively.
195 The stronger wind turning existing in the lowest few kilometres of the atmosphere is expected,
196 being probably due to boundary layer processes.

197 Figure 1b shows the location of the turbulence reports associated with the atmospheric condi-
198 tions presented in Fig. 2. These reports were issued between 2 hours before and 1 hour after 00
199 UTC of 7th February 2015. Table 1 provides details about the turbulence encounters such as type,
200 altitude, time of occurrence, intensity of the turbulence, and the cubic root of the eddy dissipation
201 rate ($\epsilon^{1/3}$ – a standard measure of CAT) estimated from on-board data (Sharman et al. 2014).

202 *b. Numerical simulations*

203 The selected day was investigated by performing semi-idealized numerical simulations using the
204 WRF-ARW atmospheric model (Skamarock and Klemp 2008). In this paper, by “semi-idealized
205 simulations” we mean simulations performed by running the WRF model in an idealized set-up,
206 but using as input data real orography (truncated as explained next) and a real atmospheric profile.
207 Note that, as discussed in the Introduction, the aim of the present paper is to assess whether the
208 ingredients necessary for triggering mountain wave breaking in the presence of directional wind
209 shear existed for the atmospheric (and lower boundary) conditions under consideration. Therefore,
210 this study does not attempt to simulate the full complexity of the flow on 7 February 2015 and of

211 the associated turbulence events, for which detailed 3D weather fields and simulations with full
212 physics (i.e., including a range of parametrizations) should be run.

213 The simulations used the model’s dynamical core only (i.e. no parametrizations), and the flow
214 was assumed to be adiabatic (no heat or moisture fluxes from the surface) and inviscid (no explicit
215 diffusion and no planetary boundary layer). Furthermore, the Coriolis force was neglected (these
216 two latter choices are justified below). The top of the model domain was at 25 km, and a 7 km-deep
217 Rayleigh damping layer was used to control wave reflection from the upper boundary.

218 An isotropic horizontal grid spacing of $\Delta x = \Delta y = 1$ km was used, and the model’s vertical
219 grid comprised 100 stretched eta levels, corresponding (approximately) to equally-spaced z -levels
220 ($\Delta z = 250$ m). With this resolution, we can expect the dominant mountain waves to be suffi-
221 ciently well-resolved by the model. Indeed, the dominant vertical wavelength of the gravity waves
222 launched by the Rocky Mountains may be estimated using a 2D hydrostatic approximation as
223 $\lambda_z \approx 2\pi U / N \approx 6$ km, if we take as representative values $N=0.01$ s^{-1} and $U = 10$ $m s^{-1}$. The
224 choice of representative background wind speed is difficult, as will be discussed in more detail in
225 section 4 (Test 3), because the wind speed varies between 7 $m s^{-1}$ and 16 $m s^{-1}$ in the lowest 3
226 km of the atmosphere. Even considering the lowest and highest values in the range of wind speed
227 variation, which correspond to $\lambda_z \approx 4$ km and $\lambda_z \approx 10$ km respectively, we can still expect to re-
228 solve the dominant mountain waves extremely well. Since from linear theory, in directional shear
229 flows the vertical wavelength of wave components with critical levels becomes indefinitely small,
230 the vertical resolution might be a more serious limitation than suggested by these rough estimates.
231 However, because wave breaking happens in physical space and this singular behaviour at critical
232 levels occurs in spectral space, a range of scales is actually involved in a given wave-breaking
233 event. The numerical simulations of Guarino et al. (2016) (using a comparable vertical resolu-

234 tion) suggest that such resolutions are sufficient to capture the smallest scales in flow overturning
235 regions (see their figure 5).

236 Each model simulation lasted 10 hours and model outputs were stored every 15 minutes. Be-
237 cause of the idealized model configuration and the relatively small domain used (see below), a
238 spin-up time of 1 hour was found to be sufficient for sound waves to leave the computational
239 domain (their speed is $\approx 1000 \text{ km h}^{-1}$) and for a quasi-stationary mountain wave field to be es-
240 tablished.

241 The model was initialized using the wind profile and the atmospheric stability profile shown in
242 Fig. 2. A portion of the Rocky Mountains range (the rectangular area in Fig. 1), downstream
243 of the Grand Junction meteorological station (for the predominant flow direction), with a (zonal)
244 length of 223 km and a (meridional) width of 144 km was chosen as the lower boundary condition.
245 The terrain elevation data come from the U.S. Geological Survey 1 arc-second resolution national
246 elevation dataset (NED), resampled to 1 km. Open lateral boundary conditions were used. The real
247 orography was placed approximately in the middle of the computational domain in order to avoid
248 steep terrain at the lateral boundaries. Numerical instability arising from high vertical velocities
249 as the incoming flow moves from flat to steep terrain was avoided by applying a smoothing along
250 the edges of the topography. In particular, 10 grid-points were used to smooth the terrain elevation
251 departing from the edge of the topography. The total size of the simulation domain is $400 \times 400 \text{ km}$.
252 Although by choosing such a large mountainous region as a forcing the effects of the Coriolis force
253 on the dynamics of mountain waves may become important ($af/U \gtrsim 1$, where a is a characteristic
254 mountain half-width, f is the Coriolis parameter and U is a velocity scale for the background
255 wind), in this study rotation effects are neglected (by imposing $f = 0$). The ambiguous definition
256 of mountain width in this case with complex terrain makes af/U difficult to estimate. af/U is
257 much less than 1 if calculated taking into account a typical value for the width of single peaks in

258 the mountain range (i.e. $a = 10$ km, following Doyle et al. (2000)), but on the contrary, is large
259 and greater than 1 if calculated considering the mountainous region as a whole (i.e. $a \approx 100$ km).

260 In order to assess to what extent the presence of the Earth's rotation can influence the generation
261 and propagation of mountain waves, a simulation in which the Coriolis force was allowed to act
262 on the flow perturbations was run. Although some discrepancies were found between the two
263 experiments with and without Earth's rotation, the overall flow pattern and, most importantly, the
264 location of flow instability regions was only marginally affected. This in principle means that
265 for our purposes the effect of the small-scale individual mountains is dominant, and that for the
266 semi-idealized simulations presented here rotation effects are nearly negligible.

267 The neglect of diffusion implied by not using a turbulence closure aims to address an initially
268 laminar state of the atmosphere from which turbulence arises as a consequence static and dynamic
269 instabilities due to wave steepening and breaking. Neglecting the PBL may seem a radical ap-
270 proach, but additional simulations (not shown) using the YSU PBL parametrization showed that
271 results did not change appreciably. Although the regions of flow instability were confined to a
272 smaller region, they occupied essentially the same positions in space and were characterized by
273 similar values of the Richardson number. An advantage of inviscid simulations is that they avoid
274 the uncertainty associated with PBL parametrizations, which are known to be especially question-
275 able over mountainous terrain (DeWekker and Kossmann 2015).

276 The model set-up described above was used for all performed simulations, including the sen-
277 sitivity tests presented in the next section. Variations made to this initial configuration for each
278 sensitivity test (i.e. changes in the orography, wind and stability profiles) will be described in the
279 results section that follows.

280 4. Results and discussion

281 a. Semi-idealized simulations: real atmospheric sounding and orography

282 Instabilities generated within the computational domain were detected by looking at fields such
283 as the potential temperature, the magnitude of the wave horizontal velocity perturbation vector
284 (u', v') , and the Richardson number of the total flow including the wave perturbation, Ri_{out} . The
285 Richardson number was calculated at each model grid-point using centered finite differences. Be-
286 cause the model vertical resolution is such that mountain waves are sufficiently well resolved (see
287 section 3b for details), the Ri field is expected to be well resolved too. Indeed, because of the
288 idealized nature of the simulations presented here, mountain wave propagation and breaking are
289 the only reason for the modulation of Ri . Note that since the simulations are inviscid, and thus
290 no turbulence parametrizations are used, Ri_{out} values of less than 0.25 and/or zero are used to
291 detect dynamical ($Ri_{out} < 0.25$) and convective ($Ri_{out} < 0$) instability regions that can potentially
292 evolve into turbulence. Ri_{out} values from inviscid simulations provide information on how close
293 the flow can get to instability, without being affected by the parametrized turbulent mixing that
294 would immediately act to restore the flow stability and neutralize layers with $N^2 < 0$.

295 Figure 3a shows the grid points in the computational domain where Ri_{out} is lower than 0.25.
296 The $Ri_{out} \leq 0.25$ field was computed between 4 and 18 km, which corresponds (approximately)
297 to the region between the height of the highest mountain peak and the height of the sponge layer
298 employed in the simulations. The first 4 km of the atmosphere were excluded from the analy-
299 sis because of unrealistic atmosphere-ground interactions that develop in frictionless simulations,
300 leading to low Ri values just above the ground (see Guarino et al. (2016)). As shown in Fig.3a,
301 low Ri values occur just above the mountain peaks (in relation, perhaps, to the aforementioned
302 atmosphere-ground interactions), between 6.5 and 10 km, and between 15 and 18 km height.

303 While the highest-level instabilities occur in the stratosphere and therefore no pilot reports are
304 available for validation purposes (aircraft cruise altitudes are usually up to about 12 km), the re-
305 gion of low Ri values located between 6.5 km and 10 km shows good agreement with the PIREPs
306 database. Indeed, most of the turbulence reports indicate turbulence occurrence between 6 km and
307 7.5 km (see Table 1).

308 In Fig.4a contours of negative values of Ri_{out} (indicating flow overturning) at $z \approx 7.5$ km are
309 shown. The background field is the terrain elevation. It can be seen that the location of the wave
310 breaking event between 6 km and 7.5 km heights, mentioned above, agrees well with the turbu-
311 lence report number 1 marked in Fig.1b (ModT1 in Table 1), both in the vertical and horizontal
312 directions.

313 In the following sub-sections, attention will be focused on analysing to what extent directional
314 wind shear is primarily responsible for the wave breaking event displayed in Fig.4a (note that at
315 different simulation times and at different locations we can observe more wave breaking events;
316 however, as the availability of PIREPs is dictated by the flight routes, there are no turbulence
317 reports directly linkable to those events).

318 *b. Sensitivity tests*

319 Despite the simplicity of the semi-idealized simulations performed, wave breaking events de-
320 tected in the simulation domain cannot be automatically associated to the presence of directional
321 wind shear. Indeed, at least three other possible environmental conditions able to modulate the
322 gravity wave amplitude can be identified: 1. a sufficiently high or steep orography; 2. the vari-
323 ation of N with height, in particular at the tropopause; 3. the speed shear in the wind profile.
324 Sensitivity tests were performed to investigate the role of each of these physical mechanisms sep-
325 arately. Note that the unsteady nature of the flow in a wave breaking event makes comparisons

326 between the simulations more difficult, since the evolution of two flows can be similar but asyn-
327 chronous. The results presented next were analysed through the use of animations of the studied
328 quantities over time, and the snap-shots presented in this paper are representative of the overall
329 flow features detected.

330 1) TEST 1: THE BOTTOM BOUNDARY CONDITION / SURFACE FORCING

331 The mechanism responsible for wave breaking in directional shear flows is sensitive to the bot-
332 tom boundary condition (as shown by (2)), which may play a crucial role in the wave breaking
333 process. We can hypothesize that orographies with different shapes, heights and orientations will
334 excite waves with high energy at wave-numbers that have critical levels at different heights, or
335 will interact with a given critical level (i.e. at a similar height) in a different way, depending
336 on the spectral energy distribution (see section 2, or Guarino et al. (2016) for a more extended
337 discussion).

338 In order to test the role of the lower boundary condition, two simulations with the same realistic
339 input sounding presented in section 3 but idealized orographies were run. More specifically, the
340 first sensitivity test was performed using an axisymmetric bell-shaped mountain given by:

$$h(x,y) = \frac{H}{\left(\frac{x^2}{a^2} + \frac{y^2}{a^2} + 1\right)^{3/2}} \quad (6)$$

341 where, following Doyle et al. (2000), the mountain height is $H = 2$ km and its half-width is $a =$
342 10 km, which are typical values for the Colorado Front Range (Doyle et al. 2000). Note that a
343 mountain height of 2 km is consistent with the mountain prominence relative to the surrounding
344 terrain as seen by the incoming flow in the realistic orography simulation, because the GJ station
345 used to initialize the model is located at about 1.5 km above sea level. Unlike Doyle et al. (2000),
346 who modelled the Rocky Mountains using an idealized 2D ridge, in this experiment a 3D mountain

347 is adopted. While it could be argued that a two-dimensional representation of the Rocky Mountains
 348 could provide a more realistic approximation to their large-scale structure, here we are interested
 349 in how the smaller-scale structure, which is intrinsically 3D, affects wave breaking, via fulfilment
 350 of the $\mathbf{U} \cdot \boldsymbol{\kappa}_H = 0$ condition. In the case of a (perfect) 2D orography with $l = 0$ the definition of
 351 critical level reduces to the one valid in unidirectional flows. However, the realistic orography
 352 considered here will certainly excite waves with wave-number vectors spanning various directions
 353 (i.e. $l \neq 0$), so use of a 3D idealized mountain is justified. Furthermore, the horizontal propagation
 354 of 3D mountain waves affect the wave amplitude, and thus the likeliness of wave breaking and
 355 turbulence occurrence, as discussed in Eckermann et al. (2015) and Xu et al. (2017).

356 For the second sensitivity test, an idealized 3D mountain ridge containing a few peaks (Martin
 357 and Lott 2007) was used:

$$h(x, y) = H e^{-[(x/a_{rdg})^2 + (y/a_{rdg})^2]} [1 + \cos(k_s x + l_s y)] \quad (7)$$

358 where the height of the highest peak in the mountain ridge is $H = 2$ km, the characteristic horizontal
 359 length-scale of the orography envelope is $a_{rdg} = 50$ km and k_s and l_s , the horizontal wave-numbers
 360 of the smaller-scale orography, have been chosen so that the half-width of each peak (defined
 361 as the distance from the peak where the terrain elevation is half its maximum) is 10 km. From
 362 visual inspection, this reproduces reasonably well the dominant smaller scales present in the real
 363 orography. The orography profile defined using the above parameters extends over an area of
 364 approximately 180×130 km, is oriented northwest-southeast and contains 5 peaks (see Fig.3b).

365 Although still drastically idealized, this orography approximates better the surface forcing im-
 366 posed by the Rocky Mountains in terms of spatial extent (the fraction of the Rocky Mountains
 367 considered in this study extends over an area of about 220×150 km), the ridges' orientation
 368 (in particular of those peaks near which turbulence was observed, according to turbulence re-

369 port number 1) and introduces a range of scales that attempts to (partially) reproduce the many
370 smaller-scale features of the real orography. Using this approach, the interaction between different
371 wave-numbers excited by the orography can be taken into account.

372 In Fig.3b and 3c the $Ri_{out} \leq 0.25$ field obtained for the two idealized orography simulations
373 is shown and compared to that obtained for the real orography simulation (Fig.3a). When an
374 isolated mountain is used (Fig.3c), despite the idealized simulation set-up, the model is able to
375 reproduce the occurrence of dynamical instabilities at higher levels in the atmosphere, but fails to
376 predict the true location of the observed instability region. Indeed, most of the turbulence reports
377 indicate turbulence between 6 km and 7.5 km (Table 1) while, in this simulation, instabilities
378 take place in a thin layer between ≈ 9.3 km and 10 km. Furthermore, taking a closer look at
379 the Ri_{out} field reveals that no negative Ri_{out} values exist, so no flow overturning due to wave
380 breaking is taking place in the simulation domain. However, when a mountain ridge with a few
381 peaks is used (Fig.3b) the instability region is wider and more pronounced, contains negative
382 Ri_{out} values and, most importantly, resembles better the flow simulated using the real orography
383 (Fig.3a). Flow instabilities occur at lower levels (≈ 4 km), between 7.5 km and 11.5 km (showing
384 a better agreement with the observations), and also at higher altitudes ($\approx 14.5 - 16.5$ km).

385 We can conclude that there is overall a poor agreement between these idealized simulations
386 and the PIREPs, but significant improvements are observed when an orography profile with a few
387 peaks is considered. This is a consequence of the fact that, although we still retain some elements
388 needed to generate mountain waves that may break in directional wind shear (namely: a stably
389 stratified atmosphere, representative values of mountain height and width, and a wind direction that
390 changes with height), the wave solution obviously depends on the Fourier transform of the terrain
391 elevation $\hat{h}(k, l)$ (see equation (2)). Hence, the energy associated to each wave-number excited at
392 the surface is closely linked to the shape and orientation of the mountain profile. Consequently, the

393 wave spectrum excited by an axisymmetric mountain, or an idealized mountain range, and by the
394 realistic orography are quite different and the interaction between wave-numbers and directional
395 critical levels differs accordingly.

396 2) TEST 2: THE TROPOPAUSE AND THE VARIATION OF N WITH HEIGHT

397 Previous studies (Worthington 1998; Whiteway et al. 2003; McHugh and Sharman 2013) pointed
398 out how the interaction between vertically propagating orographic waves and the tropopause may
399 trigger wave breaking and thus high-level turbulence generation. Furthermore, inhomogeneities
400 in the atmospheric stability can cause wave reflection (Queney 1947) that, by constructive or
401 destructive interferences between upward and downward propagating waves, can modulate the
402 surface drag and the wave amplitude itself (Leutbecher 2001). Similar wave modulations and
403 modifications of the wave-breaking conditions may be produced by sharp vertical variations in the
404 background flow shear (Teixeira and Miranda 2005).

405 Although the investigated turbulence encounter was reported at a height of about 7.3 km, and
406 therefore it is quite distant from the tropopause (in Fig.2c a substantial increase in N^2 that may
407 be identified as the tropopause occurs at about 11 km), a simulation without the tropopause, more
408 specifically assuming a constant $N = 0.01s^{-1}$, was run. The aim of this simulation was to exclude
409 as a possible cause for wave breaking the existence of significant wave reflections that could po-
410 tentially take place not only due to the high value of N at the tropopause itself, but also due to the
411 variation of N within the troposphere. This latter effect might also lead to substantial modulation
412 of the wave amplitude by refraction (according to (2),(4)-(5)).

413 In Fig.5 vertical (west-east) cross-sections of the magnitude of the wave horizontal velocity per-
414 turbation vector (u', v') are shown. The cross-sections pass through the grid-point where turbulence
415 was reported ($Y = 180$ km in Fig.4a), and the black contours delimit the regions where Ri_{out} is neg-

416 ative. Figure 5a refers to the real sounding simulation and Fig.5b to the simulation with a constant
417 N . The studied wave breaking event, responsible for the negative Ri_{out} values between 6.5 and
418 10 km, is present in both simulations. Although in Fig.5b the instability regions are smaller, they
419 present the same wake structure (discussed later in this section) visible in Fig.5a where patches of
420 negative Ri_{out} propagate downstream. Also, at the same height, the (u', v') magnitude has a very
421 similar pattern (and value) in both flows.

422 This result indicates that wave reflection is probably not significant enough to cause wave break-
423 ing. However, the large stability jump at the tropopause cannot be ignored, and wave reflection
424 is still expected to occur to some degree. An estimation of how much reflection should be ex-
425 pected for the stability profile in Fig.2b can be obtained by calculating the reflection coefficient R
426 $= (N_2 - N_1 / N_2 + N_1)$, proposed by Leutbecher (2001) for 2D flows, where we omit the minus sign
427 included by Leutbecher to make R positive. This expression for R is valid for waves travelling
428 in layers with constant N_1 and N_2 . Since in the sounding of Fig.2b, N^2 varies substantially, the
429 values of N_1 and N_2 adopted here must be understood as averages below and above the large N
430 maximum that corresponds to the tropopause, respectively. Taking $N_1 = 0.01 \text{ s}^{-1}$ at $z = 10 \text{ km}$ and
431 $N_2 = 0.02 \text{ s}^{-1}$ at $z = 11.2 \text{ km}$, we note that these are quite typical values for the troposphere and
432 stratosphere and correspond to $R = 1/3$. Therefore, we can expect that about one-third of the up-
433 ward propagating mountain waves be reflected back at the tropopause. However, in order for this
434 reflection to cause wave enhancement, the phase of the reflected wave must also be properly tuned
435 (Leutbecher 2001). The N maximum at the tropopause could also lead to horizontally propagating
436 waves trapped at that height (Teixeira et al. 2017), but since those waves decay exponentially in
437 the vertical, their effect at $z \approx 6 - 7 \text{ km}$ should be relatively modest. Hence, consistent with Fig.5b,
438 these do not seem to be the dominant mechanisms causing wave breaking.

439 The analysis presented above suggests that the effects of the tropopause and of the N variation
440 in general do not play an important role in causing the observed turbulence and, thus, are not of
441 key relevance to the event under investigation.

442 3) TEST 3: THE SPEED SHEAR

443 Alongside with the variation of N with height, the change of wind speed with height represents
444 an additional factor able to modulate the amplitude of gravity waves (see (2), (4)-(5)). In partic-
445 ular, it is known (and consistent with (4)-(5)) that a decreasing wind speed with height represents
446 the best condition for wave steepening (Smith (1977),McFarlane (1987), Sharman et al. (2012)),
447 which can facilitate the breaking of already large-amplitude waves. As can be seen in Fig.2b,
448 overall, the speed shear is positive over most of the troposphere, where the wind speed tends to
449 increase with height, however regions where the wind speed decreases with height are also present.

450 The speed shear contribution was eliminated by modifying the input wind profile so that the u
451 and v components varied with height accounting only for the observed change in the wind direc-
452 tion, neglecting the variation due to the changes in wind speed, which was kept fixed at 10 m s^{-1} .
453 The large wind speed variation for the specific day under consideration did not make it easy to
454 identify a dominant wind speed. Indeed, while the wind speed of the flow crossing the mountain
455 between 2.2 km and 3.6 km altitude varies in the range $7 \text{ m s}^{-1} - 16 \text{ m s}^{-1}$, the wind speed over
456 the mountain peaks is about 20 m s^{-1} . The value 10 m s^{-1} was chosen because it approximates
457 better the wind speed at low levels, which is presumably responsible for generating the waves (see
458 also Test 4, in the following section, where this assumption is further tested).

459 In Fig.4b the $Ri_{out} < 0$ field at $z \approx 7.5 \text{ km}$ for the new simulation including only directional
460 wind shear is shown. Both in Fig.4a (the real sounding simulation) and 4b overturning regions
461 with approximately the same location and having the same elongated shape are visible. Figure 6a

462 and 6b show again contours of negative values of Ri_{out} in west-east vertical cross-sections passing
463 through the point where turbulence was reported ($Y = 180$ km in Fig.4a). Figure 6a corresponds to
464 the simulation with the real input sounding, Fig.6c to the simulation without speed shear. Figure
465 6b and 6d show the same comparison but for the potential temperature fields. From Fig.6 we can
466 see that the wave breaking region occurs in the two simulations at similar altitudes (between 6 and
467 10 km).

468 Despite some differences between the two simulations (note that by modifying the input sound-
469 ing we are modifying the background state in which the waves are generated), the occurrence of
470 wave breaking does not seem to be related to the presence of speed shear.

471 A second test was performed to further assess the speed shear contribution to wave breaking.
472 The input wind profile was again modified but this time the u and v components varied with
473 height accounting only for the observed wind speed variation, and the directional wind shear was
474 eliminated by using a constant wind direction (chosen as a “dominant wind direction” taken by
475 inspection of the atmospheric sounding in Fig.2a as 260 degrees).

476 In Fig.5a and Fig.5c vertical cross-sections for the real sounding simulation (a) and the speed
477 shear only simulation (c) are shown. The background field is the magnitude of the horizontal
478 velocity perturbation vector (u', v') , and the black contours delimit the region with $Ri_{out} < 0$. In
479 Fig.5a waves break at an altitude of about 7 km, as discussed in section 4a. When directional
480 wind shear is removed (Fig.5c) no overturning regions where $Ri_{out} < 0$ are observed within the
481 troposphere (and lower stratosphere). However, in the speed shear only simulation, wave breaking
482 at $z \approx 15$ km – 17 km is intensified and here the magnitude of the (u', v') vector increases up to 40
483 m s^{-1} .

484 The atmospheric sounding in Fig.2b shows a net decrease of the wind speed with height in the
485 layer 14 km – 18 km. This significant negative wind shear is probably responsible for the high-

486 altitude wave breaking. In the absence of directional wind shear, the filtering of the waves at lower
487 levels is removed and all the wave-numbers in the wave spectrum break at essentially the same
488 height. Thus, the wave energy is dissipated in a thin layer, rather than over the entire troposphere,
489 resulting in the larger velocity perturbations observed in Fig.5c.

490 4) TEST 4: THE MOUNTAIN AMPLITUDE

491 A last test was necessary to verify our hypothesis that waves are breaking because of critical
492 levels imposed by the variation of the wind direction with height, and not only because of a highly
493 non-linear boundary condition such as is imposed by the Rocky Mountains. Indeed, for NH/U
494 values larger than 1, linear theory breaks down and wave breaking is expected to occur even in
495 unsheared flows (Huppert and Miles (1969), Smith (1980), Miranda and James (1992)).

496 For this purpose, simulations in which both wind speed and direction are kept constant were
497 performed. In these simulations the wind direction was again set to 260 degrees and we used two
498 different values of wind speed: $U = 10 \text{ m s}^{-1}$ and $U = 20 \text{ m s}^{-1}$. As discussed in the previous
499 section, the choice of a representative wind speed of the flow passing over the orography is difficult
500 because of the large variation of U in the lowest 3.5 km of the atmosphere. In the sensitivity tests
501 presented here, 10 m s^{-1} was used because it was assumed to be representative of the flow at lower
502 levels, while 20 m s^{-1} was used to test the robustness of this assumption, and also because it is the
503 wind speed just above the highest mountain peaks.

504 Fig.5d compares the $U = 10 \text{ m s}^{-1}$ simulation with the real sounding simulation of Fig.5a.
505 While in Fig.5a the breaking region is again easily detected between 7 and 10 km, where patches
506 of negative values of the Richardson number appear, for the simulation with a constant wind speed
507 and direction (Fig.5d), the waves continue to propagate upwards without breaking at the same
508 heights and horizontal locations.

509 This ability of the gravity waves to propagate to higher levels in the atmosphere supports the
510 argument that, by removing the directional wind shear, we removed the mechanism responsible
511 for wave breaking in the event under consideration (this test also directly compares with Test 3,
512 Fig.4b, where $U = 10 \text{ m s}^{-1}$ and directional wind shear is present). More specifically, without
513 directional wind shear, the filtering of the wave energy by critical levels vanishes. Therefore,
514 wave-numbers that would otherwise be absorbed into the mean flow, or increase their amplitude
515 and cause wave breaking, remain essentially unaffected and keep on propagating upward.

516 In addition to vertically propagating gravity waves, in Fig.5d, a few instability regions are also
517 visible, but not at the correct levels. The mechanism behind these instabilities, and the associated
518 wave breaking, can only be related to the high amplitude of the surface forcing provided by the
519 Rocky Mountains, conjugated with the decrease of density with height (which are the only possible
520 wave breaking mechanisms active in this case).

521 When $U = 20 \text{ m s}^{-1}$ is assumed (Fig.5e), large amplitude gravity waves are excited by the Rocky
522 Mountains that break vigorously (the maximum on the $|(u', v')|$ scale is 34 m s^{-1}) both at lower
523 and higher atmospheric levels.

524 The opposite flow behaviour observed in the two tests is a consequence of the transition between
525 two well known different flow regimes. Assuming $N = 0.01 \text{ s}^{-1}$ and $H = 2 \text{ km}$, which is a good
526 estimate of the mountain height as seen by the incoming flow (the GJ station used to initialize the
527 model is located at about 1.5 km above sea level), $NH/U = 2$ when $U = 10 \text{ m s}^{-1}$ and NH/U
528 $= 1$ when $U = 20 \text{ m s}^{-1}$. For a 3D orography, when $NH/U = 2$ the flow enters a “flow around”
529 regime for which a significant part of the flow is deflected around the flanks of the obstacle and
530 the generation of vertically propagating mountain waves is weakened. When $NH/U = 1$ most of
531 the incoming flow passes over the orography and wave breaking is favoured (Miranda and James
532 1992).

533 In reality, the amplitude of the waves excited by the Rocky Mountains will be the result of a
534 varying wind speed, and not of a fixed U . Therefore, although the flow simulated using $U = 10 \text{ m}$
535 s^{-1} is closer to the one in Fig.5a in terms of magnitude of the velocity perturbation vector, the wave
536 breaking found when $U = 20 \text{ m s}^{-1}$ suggests that the effective wind speed of the flow approach-
537 ing the mountain can be decisive in causing wave breaking. We conclude that it is not possible
538 to exclude self-induced overturning from the possible wave breaking mechanisms. Instead, this
539 mechanism is probably acting alongside the directional wind shear mechanism (as discussed in
540 more detail in the following section).

541 *c. The directional wind shear contribution*

542 While Tests 2, 3 and 4 investigated the role of static stability, speed shear and mountain height
543 in causing the studied turbulence encounter, in this section more direct evidence that waves may
544 break because of environmental critical levels associated with the presence of the directional wind
545 shear will be presented and discussed.

546 Both in the horizontal cross-section of Fig.4 and in the vertical cross-section of Fig.5a, the region
547 corresponding to $Ri_{out} < 0$ exhibits an elongated shape that, departing from the first wave breaking
548 point, extends downstream forming a certain (small) angle with the wind direction (which is very
549 close to 270 degrees) at that height. This downwind transport of statically unstable air seems to
550 be a signature of breaking waves in directional shear flows. Based on linear theory arguments,
551 Shutts (1998) demonstrated the existence of a flow feature known as “asymptotic wake” (see also
552 Shutts and Gadian (1999)). The asymptotic wake is a consequence of wave-numbers approaching
553 critical levels in directional shear flows and, more precisely, of a component of the background
554 wind parallel to the wave phase lines that will advect the wave energy away from the mountain (in
555 stationary conditions).

556 The asymptotic wake predicted by Shutts translates into lobes of maximum wave velocity pertur-
557 bation extending along the wind direction at each height, but not perfectly aligned with it (Fig.7a).
558 Steady linear theory predicts that shear will become indefinitely large in these flow regions. We
559 speculate that the tail of negative Ri values in Figs. 4 and 5a, which is absent in all the breaking
560 regions in Test 4 (see for example Fig.5d), is a manifestation of the asymptotic wake predicted
561 by Shutts (1998). Although the asymptotic wake is a feature of steady flow, it develops due to
562 advection of the wave field by the wind at critical levels, which means that it can extend over long
563 distances in short time intervals, even when the flow is not perfectly steady.

564 In Fig.7 the magnitude of the horizontal velocity perturbation vector (u', v') is shown for 5 dif-
565 ferent cases:

566 • Figure 7a and 7b show the flow behaviour for orographic waves excited by an axisymmet-
567 ric mountain (as described by (6)) in the case of a background wind direction that changes
568 (backs) continuously with height (constant rate of rotation ≈ 14 degrees/km), a constant $N =$
569 0.01 s^{-1} and wind speed $U = 10 \text{ m s}^{-1}$. Fig.7a shows the analytical solution obtained from
570 a linear model for such a flow, similar to that developed by Teixeira and Miranda (2009), in
571 Fig.7b the corresponding idealized numerical simulation (with $H = 1 \text{ km}$) is presented. The
572 numerical set-up for this idealized simulation is slightly different from the one presented in
573 section 3 (see Guarino et al. (2016) for further details).

574 • Figure 7c and 7d correspond to Test 1, therefore they depict simulations that use an idealized
575 3D orography (as described by (6)) and a set of idealized mountain ridges (as described by
576 (7)) but a real atmospheric sounding.

577 • Figure 7e corresponds to the semi-idealized simulation that uses real orography and a real at-
578 mospheric sounding (more specifically, it focuses on a portion of the entire simulation domain
579 shown in Fig.4a, starting at $X = 240$ km, $Y = 110$ km).

580 The black contours are the lowest Ri_{out} values for each simulation. Note that although in Fig.7a
581 and 7b the wind rotates counter-clockwise and in Fig.7c, 7d and 7e it rotates clockwise, this
582 only modifies the quadrants in which the wave energy is advected at different heights (and so
583 where the maximum of the wave perturbation field is), and the two sets of results may be seen
584 as essentially equivalent via mirror and rotation transformations. The purpose of Fig.7 is to show
585 the progressive transition of the asymptotic wake structure as the degree of realism of the flow
586 increases. The asymmetry of the wave perturbation field is visible in both Fig.7a and 7b, where
587 the left-hand branch extends to the north-west, approaching asymptotically the wind direction at
588 that height (this is the asymptotic wake). As we shift towards less idealized flows (Fig.7c, 7d and
589 7e), this flow feature becomes less clear but it is still detectable (albeit mirrored).

590 Proving the existence of the asymptotic wake in real case studies is of a particular interest, since
591 approximately hydrostatic mountain waves (such as the ones excited by the Rocky Mountains)
592 are usually expected to break and cause turbulence just above the mountain peaks and not far
593 downstream, but this is what seems to happen when an asymptotic wake is present (see in particular
594 Fig.5a).

595 1) SPECTRAL ANALYSIS OF THE WAVE FIELD

596 A final piece of evidence supporting the importance of critical levels due to directional wind
597 shear is provided by spectral analysis carried out on the magnitude of the (u', v') field. The quan-
598 tity (u', v') was chosen because of the strong amplification of the horizontal velocity perturbations
599 at critical levels (Guarino et al. 2016). This spectral analysis will be first presented for the the fully

600 idealized simulation (with an idealized axisymmetric orography and idealized atmospheric sound-
601 ing) introduced in the previous section, and then for the more realistic case being investigated.

602 In Fig.8¹ the 2D spatial power spectra of the horizontal velocity perturbation field, computed
603 at different heights from the fully idealized simulation are shown. The five spectra correspond to
604 (u', v') horizontal cross-sections taken at 3 km, 6.1 km, 7 km, 10 km and 13 km heights, at a same
605 simulation time. Note that Fig.8c is the 2D power spectrum of Fig.7b. Since the Fourier transform
606 of a purely real signal is symmetric, in a 2D power spectrum all the information is contained in the
607 first two quadrants of the (k, l) plane and the third $(k < 0, l < 0)$ and fourth $(k > 0, l < 0)$ quadrants
608 are just mirrored images of the first $(k > 0, l > 0)$ and second $(k < 0, l > 0)$ quadrants, respectively.

609 For the idealized wind profile employed in this simulation, the continuous (and smooth) turning
610 of the background wind vector with height creates a continuous distribution of critical levels in
611 the vertical. At each critical level, the wave energy is absorbed into the background flow and
612 this absorption affects one wave-number in the spectrum at a time (i.e., at each level). Looking
613 at the power spectra in Fig.8, it can be seen that the dominant wave-number at each height (i.e.
614 that with most energy) is the one nearly perpendicular to the incoming wind (i.e. the one having
615 a critical level at that height). As a consequence, the wave-number vector of the most energetic
616 wave-mode rotates counter-clockwise following the background wind, but about 90 degrees out of
617 phase. It can also be seen that as the incoming wind rotates by a certain angle, the portion of the
618 wave spectrum corresponding to wave-numbers perpendicular to the wind at lower levels has been
619 absorbed. For example: in Fig.8b the wind is from the South, departing from a westerly surface
620 direction, so all the wave-numbers in the second quadrant $(k < 0, l > 0)$ have been absorbed. When
621 the background wind has rotated by 180 degrees (Fig.8e) practically all the wave energy has been

¹Note that in both Fig.8 and Fig.9, the non-zero spectral energies extending along the x and y axes correspond to numerical noise generated in the computation of the 2D power spectra, and so should be physically disregarded.

622 dissipated, because all possible critical levels have been encountered at lower altitudes (Teixeira
623 and Miranda 2009) (this is confirmed by flow cross-sections – not shown – where no waves exist
624 above the height where the power spectrum in Fig.8e was computed).

625 It should be noted that the angle actually detected between the background wind direction and
626 the most energetic wave-mode at each height is slightly less than 90 degrees. A plausible interpre-
627 tation is that, although a wave reaches its maximum amplitude at a critical level in linear theory,
628 this is also the height where it will break. For finite-amplitude waves, amplification and break-
629 ing tends to occur some distance below critical levels. Therefore, typically, the energy carried
630 by a wave-number vector perpendicular to the wind has already been absorbed, and so the angle
631 between wavenumbers that still carry maximum energy (prior to breaking) and the local wind di-
632 rection will be less than 90 degrees. An estimate of this effect can be obtained as follows. Taking
633 the wave amplitude at wave breaking altitude as ≈ 500 m (not shown) and multiplying this by the
634 turning rate of the background wind ≈ 14 degrees km^{-1} , a misalignment of ≈ 7 degrees is ob-
635 tained. This is at least of the same order of magnitude as the value that can be estimated visually
636 from Fig.8.

637 When similar 2D power spectra are computed for the more realistic case under consideration,
638 significant similarities can be seen. In Fig.9 the 2D spatial power spectra computed from the semi-
639 idealized numerical simulation are shown at heights comprising every kilometre of the atmosphere
640 between 5.5km and 15.5 km. Figure 9c is the 2D power spectrum of Fig.7e. The slower and
641 non-constant rate of wind turning with height characterizing this case makes it more difficult to
642 detect the rotation of the dominant wave-number following the wind. However, a rotation is still
643 revealed by the changing orientation with height of the dominant wave energy lobes in the plots.
644 In particular, approximate perpendicularity between the wind direction and the dominant wave-
645 numbers can be seen between 7.5 and 10.5 km. These are the heights where, in physical space,

646 most of the wave breaking occurs. Between 9.5 km and 10.5 km, the wind direction remains
647 essentially constant. At higher altitudes, 11.5 – 13.5 km, the wind rotation rate slows down and, as
648 a consequence, the differences between spectra become harder to distinguish. By 13.5 km, because
649 of the wave breaking taking place below and the ensuing critical level absorption, most of the wave
650 energy has been dissipated. Note that, just as in the idealized case of Fig.8, when measured more
651 precisely the angle between the incoming wind vector and the dominant wave-number vector is
652 seen to be slightly lower than 90 degrees (e.g. Fig.9g).

653 The wave behaviour inferred from the spectra in Fig.9, being essentially similar to that displayed
654 in Fig.8, is equally explained by the mechanism leading to wave breaking in directional shear
655 flows. In contrast, similar 2D power spectra computed for Test 4 (not shown), where the wind
656 direction is constant with height, display no selective wave-energy absorption as a function of
657 height.

658 A final note on the power spectra of Fig.9 concerns the modulation of the wave amplitude by
659 the variation with height of background flow parameters. The existence of additional processes
660 contributing to the wave dynamics is deducible from the power spectra computed between 9.5 km
661 and 12.5 km. Above 9.5 km the rotation of the wind slows down significantly and so it seems un-
662 likely that directional critical levels are the only reason for the high energy regions in the spectra of
663 Fig.9f, 9g and 9h. This is probably a consequence of changes in other background flow parameters
664 with height, such as stability and wind speed. It was shown in Fig.2b that the wind speed between
665 5.5 km and 9.5 km decreases from 20.6 m s^{-1} to 18 m s^{-1} . As mentioned previously (see Test 3
666 and equations (2), (4)-(5)), this type of variation can cause the wave amplitude to increase. Addi-
667 tionally, the significant increase in N^2 starting at about 11 km can cause wave reflections (see Test
668 2 and equations (2), (4)-(5)), which might also result in an enhancement of the wave amplitude
669 at lower atmospheric levels by resonance. Although sensitivity tests 2 and 3 indicate that these

670 mechanisms are not strong enough to cause wave breaking, they may still be strong enough for
671 their influence on the wave amplitude to be revealed in the power spectra of Fig.9.

672 **5. Summary and conclusions**

673 In this paper, mountain wave turbulence in the presence of directional vertical wind shear over
674 the Rocky Mountains in the state of Colorado has been investigated. For the winter seasons of
675 2015 and 2016, days with a significant directional wind shear within the upper troposphere (4
676 km – tropopause height) were identified by analysing atmospheric soundings measured upstream
677 of the Rocky Mountains at the Grand Junction meteorological station (GJT). Among these days,
678 pilot reports of turbulence encounters (PIREPs) were used to select cases where moderate or severe
679 turbulence events were reported.

680 A selected case was investigated by performing semi-idealized numerical simulations, and sen-
681 sitivity tests, aimed at discerning the contribution of mountain wave breaking due to directional
682 wind shear in the observed turbulence event. In these simulations, the WRF-ARW model was
683 initialized with a 1D atmospheric sounding from Grand Junction (CO) and a real (but truncated)
684 orography profile. The orography was modified in the sensitivity test “Test 1”, and the atmospheric
685 sounding was modified in the sensitivity tests “Test 2”, “Test 3”, “Test 4”.

686 For the simulation with a realistic atmospheric sounding and orography, low positive and nega-
687 tive Richardson number values (used to identify regions of flow instability) occurred between 6.5
688 km and 10 km, providing overall good agreement with the PIREPs.

689 In Test 1, the role of the surface forcing in causing wave breaking was investigated. In particular,
690 the lower boundary condition was modified and replaced with a 3D bell-shaped mountain and
691 an idealized orography containing a few ridges. For these experiments, overall the agreement
692 between model-predicted instabilities and PIREPs degraded. However, a better representation of

693 flow dynamical and convective instabilities was achieved when the orography with a few peaks
694 was considered. The results of Test 1 support the hypothesis that, in directional shear flows,
695 by exciting substantially different wave spectra, orographies with different shapes, heights and
696 orientations can change the nature of the wave-critical level interaction.

697 In Test 2, the effect of the tropopause and of the vertical variation of N on wave breaking were
698 tested. The real atmospheric stability profile was replaced with an idealized profile prescribed by
699 imposing a constant $N = 0.01 \text{ s}^{-1}$. Despite the constant stability, the investigated wave breaking
700 event still occurred, and the flow cross-sections showed essentially the same features observed in
701 the real-sounding simulation.

702 In Test 3, the influence of the variation of wind speed with height on wave steepening was ex-
703 plored. In a first test, the speed shear contribution was eliminated by modifying the atmospheric
704 sounding so that changes in u' and v' were due to directional wind shear only, while the wind speed
705 was kept constant at 10 m s^{-1} . In a second test, the directional wind shear contribution was elimi-
706 nated by keeping the wind direction constant with height while the observed wind speed variation
707 was retained. In the directional-shear-only simulation, the investigated turbulence encounter was
708 still present. In the speed-shear-only simulation, no overturning regions were found in the simu-
709 lation domain at $z \approx 7 \text{ km}$, where the studied turbulence encounter occurred. These tests suggest
710 that wave breaking was not likely attributable to the presence of speed shear.

711 In Test 4, the highly non-linear boundary condition imposed by the Rocky Mountains (for which
712 $NH/U = O(1)$) was studied. Both wind speed and direction were kept constant with height, but
713 two different wind speeds were used, namely: $U = 10 \text{ m s}^{-1}$ and $U = 20 \text{ m s}^{-1}$. For the 10 m s^{-1}
714 simulation, $NH/U = 2$, so mountain waves were relatively weak and propagated upwards without
715 breaking at that level where turbulence was observed. For the 20 m s^{-1} simulation, $NH/U =$
716 1 and mountain waves broke at multiple altitudes. These tests show that for the orography and

717 flow configuration under investigation, wave breaking is quite sensitive to the wind speed of the
718 incoming flow. The large variation of U in the lowest kilometres of the atmosphere does not
719 allow us to exclude self-induced overturning as a possible wave breaking mechanism. Instead, this
720 mechanism probably coexists with the directional wind shear, which acts to localize vertically the
721 wave breaking regions.

722 In connection with the studied wave breaking event, a significant downwind transport of unsta-
723 ble air was detected in horizontal cross-sections of the flow. This allows mountain-wave-induced
724 turbulence to be found at large horizontal distances from the orography that generates the waves.
725 A possible explanation for the observed flow pattern is the existence of an “asymptotic wake”,
726 as predicted by Shutts (1998) using linear theory for waves approaching critical levels in direc-
727 tional shear flows. The asymptotic wake translates into lobes of maximum wave energy extending
728 roughly along the wind direction at a particular height, but not perfectly aligned with the wind.
729 This peculiar flow structure was displayed by the horizontal velocity perturbation field (u', v') in
730 horizontal cross-sections of the simulated flow.

731 Critical levels associated with directional wind shear were further investigated using spectral
732 analysis of the magnitude of the (u', v') vector. This was done for a fully idealized flow and for the
733 more realistic flow that is the main focus of the present paper. Power spectra of the horizontal ve-
734 locity perturbation at different heights and changes in the corresponding wave energy distribution
735 by wavenumber (i.e. wave energy absorption/enhancement) were analysed.

736 For the fully idealized simulation, the continuous distribution of critical levels in the vertical
737 makes the dominant wave-number vector at each height be (almost) perpendicular to the back-
738 ground wind vector at that height. As a result, the wave-number vector of the most energetic
739 wave-mode rotates counter-clockwise, following the background wind 90 degrees out of phase.
740 The implications of this for the approximate perpendicularity between the background wind vec-

741 tor and the wave velocity perturbation vector at critical levels is discussed by Guarino et al. (2016).
742 For the semi-idealized simulation, it was still possible to detect a rotation of the dominant wave-
743 number with the wind, even if less clearly than in the idealized case. In particular, the wind
744 direction and the dominant wave-number were seen to be approximately perpendicular between
745 7.5 and 10.5 km where most of the wave breaking occurs in physical space.

746 The experiments discussed in this paper suggest that critical levels induced by directional wind
747 shear played a crucial role in originating the investigated turbulence encounter (ModTurb1 in Ta-
748 ble 1). The directional wind shear contribution to wave breaking dynamics is particularly relevant
749 to the problem of how the wave energy is selectively absorbed or dissipated at critical levels,
750 which also has implications for drag parametrization (Teixeira and Yu 2014). Furthermore, direc-
751 tional wind shear produces regions of flow instability far downwind from the obstacle generating
752 the waves. This is a non-trivial result, especially for hydrostatic mountain waves, which are ex-
753 pected to propagate essentially vertically, and are therefore treated in drag parametrizations using
754 a single-column approach. This downstream propagation of instabilities, which is a manifestation
755 of the “asymptotic wake” predicted by Shutts (1998), hence represents an overlooked turbulence
756 generation mechanism that, if adequately taken in account, might improve the location accuracy
757 of mountain wave turbulence forecasts.

758 The semi-idealized approach used here was particularly well-suited to the aims of the present
759 study, as it allowed us to isolate and investigate separately different wave breaking mechanisms.
760 However, the simplifications adopted in the numerical simulations constitute a source of uncer-
761 tainty regarding the applicability of the results to real situations. Making the numerical simula-
762 tions more realistic by including missing physical processes (e.g., boundary layer effects, moisture
763 and phase transitions), would therefore be a natural next step to further understand the observed
764 turbulence event.

765 *Acknowledgments.* M.V.G. and M.A.C.T. acknowledge the financial support of the European
766 Commission under Marie Curie Career Integration Grant GLIMFLO, contract PCIG13-GA-2013-
767 618016.

768 **References**

- 769 Ágústsson, H., and H. Ólafsson, 2014: Simulations of observed lee waves and rotor turbulence.
770 *Mon. Wea. Rev.*, **142**, 832–849.
- 771 Booker, J. R., and F. P. Bretherton, 1967: The critical layer for internal gravity waves in a shear
772 flow. *J. Fluid Mech.*, **27**, 513–539.
- 773 Broad, A. S., 1995: Linear theory of momentum fluxes in 3-d flows with turning of the mean wind
774 with height. *Q. J. R. Meteorol. Soc.*, **121**, 1891–1902.
- 775 Broutman, D., S. D. Eckermann, H. Knight, and J. Ma, 2017: A stationary phase solution for
776 mountain waves with application to mesospheric mountain waves generated by auckland island.
777 *J. Geophys. Res. - Atmos.*, **122**, 699–711.
- 778 Carslaw, K. S., and Coauthors, 1998: Increased stratospheric ozone depletion due to mountain-
779 induced atmospheric waves. *Nature*, **391**, 675–678.
- 780 DeWecker, S., and M. Kossmann, 2015: Convective boundary layer heights over mountainous
781 terrain - a review of concepts. *Front. Earth Sci.*, **3**, 77.
- 782 Dörnbrack, A., T. Gerz, and U. Schumann, 1995: Turbulent breaking of overturning gravity waves
783 below a critical level. *Appl. Scient. Res.*, **54**, 163–176.
- 784 Doyle, J., and Q. Jiang, 2006: Observations and numerical simulations of mountain waves in the
785 presence of directional wind shear. *Q. J. R. Meteorol. Soc.*, **132**, 1877–1905.

- 786 Doyle, J., and Coauthors, 2000: An intercomparison of model-predicted wave breaking for the 11
787 january 1972 boulder windstorm. *Mon. Wea. Rev.*, **128**, 901–914.
- 788 Durran, D. R., 1990: Mountain waves and downslope winds. *Atmospheric processes over complex*
789 *terrain*, Springer, 59–81.
- 790 Eckermann, S. D., A. Dörnbrack, H. Flentje, S. B. Vosper, M. Mahoney, T. P. Bui, and K. S.
791 Carslaw, 2006: Mountain wave–induced polar stratospheric cloud forecasts for aircraft science
792 flights during solve/theseo 2000. *Wea. Forecast.*, **21**, 42–68.
- 793 Eckermann, S. D., J. Ma, and D. Broutman, 2015: Effects of horizontal geometrical spreading on
794 the parameterization of orographic gravity wave drag. part i: Numerical transform solutions. *J.*
795 *Atmos. Sci.*, **72**, 2330–2347.
- 796 Elvidge, A. D., S. B. Vosper, H. Wells, J. C. Cheung, S. H. Derbyshire, and D. Turp, 2017: Moving
797 towards a wave-resolved approach to forecasting mountain wave induced clear air turbulence.
798 *Meteorological Applications*, **24**, 540–550.
- 799 Gill, P. G., 2014: Objective verification of world area forecast centre clear air turbulence forecasts.
800 *Meteorol. Applic.*, **21**, 3–11.
- 801 Gill, P. G., and A. J. Stirling, 2013: Including convection in global turbulence forecasts. *Meteorol.*
802 *Applic.*, **20**, 107–114.
- 803 Grubišić, V., S. Serafin, L. Strauss, S. J. Haimov, J. R. French, and L. D. Oolman, 2015: Wave-
804 induced boundary layer separation in the lee of the medicine bow mountains. part ii: Numerical
805 modeling. *J. Atmos. Sci.*, **72**, 4865–4884.
- 806 Grubišić, V., and P. K. Smolarkiewicz, 1997: The effect of critical levels on 3d orographic flows:
807 Linear regime. *J. Atmos. Sci.*, **54**, 1943–1960.

- 808 Guarino, M.-V., M. A. Teixeira, and M. H. Ambaum, 2016: Turbulence generation by mountain
809 wave breaking in flows with directional wind shear. *Q. J. R. Meteorol. Soc.*, **142**, 2715–2726.
- 810 Huppert, H. E., and J. W. Miles, 1969: Lee waves in a stratified flow. part 3. semi-elliptical obsta-
811 cle. *J. Fluid Mech.*, **35**, 481–496.
- 812 Jiang, Q., and J. D. Doyle, 2004: Gravity wave breaking over the central alps: Role of complex
813 terrain. *J. Atmos. Sci.*, **61**, 2249–2266.
- 814 Julian, L. T., and P. R. Julian, 1969: Boulder’s winds. *Weatherwise*, **22**, 108–126.
- 815 Keller, T. L., S. B. Trier, W. D. Hall, R. D. Sharman, M. Xu, and Y. Liu, 2015: Lee waves
816 associated with a commercial jetliner accident at denver international airport. *J. Appl. Meteor.*
817 *Climatol.*, **54**, 1373–1392.
- 818 Kim, J.-H., and H.-Y. Chun, 2010: A numerical study of clear-air turbulence (cat) encounters over
819 south korea on 2 april 2007. *J. Appl. Meteor. Climatol.*, **49**, 2381–2403.
- 820 Kirshbaum, D. J., G. H. Bryan, R. Rotunno, and D. R. Durran, 2007: The triggering of orographic
821 rainbands by small-scale topography. *J. Atmos. Sci.*, **64**, 1530–1549.
- 822 Lane, T. P., J. D. Doyle, R. D. Sharman, M. A. Shapiro, and C. D. Watson, 2009: Statistics and
823 dynamics of aircraft encounters of turbulence over greenland. *Mon. Wea. Rev.*, **137**, 2687–2702.
- 824 Leutbecher, M., 2001: Surface pressure drag for hydrostatic two-layer flow over axisymmetric
825 mountains. *J. Atmos. Sci.*, **58**, 797–807.
- 826 Lilly, D. K., 1978: A severe downslope windstorm and aircraft turbulence event induced by a
827 mountain wave. *J. Atmos. Sci.*, **35**, 59–77.

- 828 Lilly, D. K., and P. J. Kennedy, 1973: Observations of a stationary mountain wave and its associ-
829 ated momentum flux and energy dissipation. *J. Atmos. Sci.*, **30**, 1135–1152.
- 830 Martin, A., and F. Lott, 2007: Synoptic responses to mountain gravity waves encountering direc-
831 tional critical levels. *J. Atmos. Sci.*, **64**, 828–848.
- 832 McFarlane, N. A., 1987: The effect of orographically excited gravity wave drag on the general
833 circulation of the lower stratosphere and troposphere. *J. Atmos. Sci.*, **44**, 1775–1800.
- 834 McHugh, J., and R. Sharman, 2013: Generation of mountain wave-induced mean flows and turbu-
835 lence near the tropopause. *Q. J. R. Meteorol. Soc.*, **139**, 1632–1642.
- 836 Miranda, P., and I. James, 1992: Non-linear three-dimensional effects on gravity-wave drag: Split-
837 ting flow and breaking waves. *Q. J. R. Meteorol. Soc.*, **118**, 1057–1081.
- 838 Nappo, C. J., 2012: *An Introduction to Atmospheric Gravity Waves, 2nd Ed.* Academic Press.
- 839 Queney, P., 1947: *Theory of perturbations in stratified currents with applications to air flow over*
840 *mountain barriers.* University of Chicago Press.
- 841 Schwartz, B., 1996: The quantitative use of pireps in developing aviation weather guidance prod-
842 ucts. *Wea. Forecast.*, **11**, 372–384.
- 843 Sharman, R., L. Cornman, G. Meymaris, J. Pearson, and T. Farrar, 2014: Description and derived
844 climatologies of automated in situ eddy-dissipation-rate reports of atmospheric turbulence. *J.*
845 *Appl. Meteor. Climatol.*, **53**, 1416–1432.
- 846 Sharman, R., and J. Pearson, 2016: Prediction of energy dissipation rates for aviation turbulence:
847 Part i. forecasting non-convective turbulence. *J. Appl. Meteor. Climatol.*, **56**, 317–337.

- 848 Sharman, R., C. Tebaldi, G. Wiener, and J. Wolff, 2006: An integrated approach to mid-and upper-
849 level turbulence forecasting. *Wea. Forecast.*, **21**, 268–287.
- 850 Sharman, R., S. Trier, T. Lane, and J. Doyle, 2012: Sources and dynamics of turbulence in the
851 upper troposphere and lower stratosphere: A review. *Geophys. Res. Lett.*, **39**.
- 852 Shutts, G., 1995: Gravity-wave drag parametrization over complex terrain: The effect of critical-
853 level absorption in directional wind-shear. *Q. J. R. Meteorol. Soc.*, **121**, 1005–1021.
- 854 Shutts, G. J., 1998: Stationary gravity-wave structure in flows with directional wind shear. *Q. J.*
855 *R. Meteorol. Soc.*, **124**, 1421–1442.
- 856 Shutts, G. J., and A. Gadian, 1999: Numerical simulations of orographic gravity waves in flows
857 which back with height. *Q. J. R. Meteorol. Soc.*, **125**, 2743–2765.
- 858 Skamarock, W. C., and J. B. Klemp, 2008: A time-split nonhydrostatic atmospheric model for
859 weather research and forecasting applications. *J. Comput. Phys.*, **227**, 3465–3485.
- 860 Smith, R. B., 1977: The steepening of hydrostatic mountain waves. *J. Atmos. Sci.*, **34**, 1634–1654.
- 861 Smith, R. B., 1980: Linear theory of stratified hydrostatic flow past an isolated mountain. *Tellus*,
862 **32**, 348–364.
- 863 Strauss, L., S. Serafin, S. Haimov, and V. Grubišić, 2015: Turbulence in breaking mountain waves
864 and atmospheric rotors estimated from airborne in situ and doppler radar measurements. *Q. J.*
865 *R. Meteorol. Soc.*, **141**, 3207–3225.
- 866 Teixeira, M., 2014: The physics of orographic gravity wave drag. *Front. Phys.*, **2**, 43.
- 867 Teixeira, M., and P. Miranda, 2005: Linear criteria for gravity-wave breaking in resonant stratified
868 flow over a ridge. *Quarterly Journal of the Royal Meteorological Society*, **131**, 1815–1820.

- 869 Teixeira, M., P. Miranda, and J. Argañ, 2008: Mountain waves in two-layer sheared flows:
870 Critical-level effects, wave reflection, and drag enhancement. *J. Atmos. Sci.*, **65**, 1912–1926.
- 871 Teixeira, M., and C. Yu, 2014: The gravity wave momentum flux in hydrostatic flow with direc-
872 tional shear over elliptical mountains. *Eur. J. Mech. B - Fluids*, **47**, 16–31.
- 873 Teixeira, M. A. C., and P. M. A. Miranda, 2009: On the momentum fluxes associated with moun-
874 tain waves in directionally sheared flows. *J. Atmos. Sci.*, **66**, 3419–3433.
- 875 Teixeira, M. A. C., P. M. A. Miranda, and M. A. Valente, 2004: An analytical model of mountain
876 wave drag for wind profiles with shear and curvature. *J. Atmos. Sci.*, **61**, 1040–1054.
- 877 Teixeira, M. A. C., A. Paci, and A. Belleudy, 2017: Drag produced by waves trapped at a density
878 interface in non-hydrostatic flow over an axisymmetric hill. *J. Atmos. Sci.*, **74**, 1839–1857.
- 879 Trier, S. B., R. D. Sharman, and T. P. Lane, 2012: Influences of moist convection on a cold-season
880 outbreak of clear-air turbulence (cat). *Mon. Wea. Rev.*, **140**, 2477–2496.
- 881 Turner, J., 1999: Development of a mountain wave turbulence prediction scheme for civil aviation.
882 Tech. Rep. 265, Met Office, Bracknell, UK.
- 883 Whiteway, J. A., E. G. Pavelin, R. Busen, J. Hacker, and S. Vosper, 2003: Airborne measurements
884 of gravity wave breaking at the tropopause. *Geophys. Res. Lett.*, **30**, 2070.
- 885 Wolff, J., and R. Sharman, 2008: Climatology of upper-level turbulence over the contiguous united
886 states. *J. Appl. Meteor. Climatol.*, **47**, 2198–2214.
- 887 Worthington, R., 1998: Tropopausal turbulence caused by the breaking of mountain waves. *J.*
888 *Atmos. Solar-terrest. Phys.*, **60**, 1543–1547.

889 Xu, X., J. Song, Y. Wang, and M. Xue, 2017: Quantifying the effect of horizontal propagation of
890 three-dimensional mountain waves on the wave momentum flux using gaussian beam approxi-
891 mation. *J. Atmos. Sci.*, **74**, 1783–1798.

892 Xu, X., Y. Wang, and M. Xue, 2012: Momentum flux and flux divergence of gravity waves in
893 directional shear flows over three-dimensional mountains. *J. Atmos. Sci.*, **69**, 3733–3744.

894 **LIST OF TABLES**

895 **Table 1.** Details about the turbulence reports, namely: type (moderate or severe
896 turbulence (ModT, SevT), moderate or severe mountain wave turbulence
897 (ModMWT, SevMWT)), time, altitude, and intensity of the turbulence, and
898 the cubic root of the eddy dissipation rate ($\epsilon^{1/3}$). 43

899 TABLE 1. Details about the turbulence reports, namely: type (moderate or severe turbulence (ModT, SevT),
 900 moderate or severe mountain wave turbulence (ModMWT, SevMWT)), time, altitude, and intensity of the tur-
 901 bulence, and the cubic root of the eddy dissipation rate ($\epsilon^{1/3}$).

| ID | Type of turbulence | Date and UTC time | Altitude (feet) | $\epsilon^{1/3}$ ($\text{m}^{2/3} \text{s}^{-1}$) |
|----|--------------------|--------------------|-----------------|---|
| 1 | ModT | 06 Feb 2015, 22.41 | 24000 | 0.50 |
| 2 | ModMWT | 06 Feb 2015, 22.57 | 22000 | 0.50 |
| 3 | SevMWT | 06 Feb 2015, 22.59 | 24000 | 0.62 |
| 4 | SevT | 06 Feb 2015, 23.47 | 24000 | 0.75 |
| 5 | SevT | 07 Feb 2015, 01.15 | 16000 | 0.75 |
| 6 | ModT | 07 Feb 2015, 01.15 | 13000 | 0.50 |
| 7 | ModT | 07 Feb 2015, 01.15 | 20000 | 0.50 |

902 **LIST OF FIGURES**

903 **Fig. 1.** (a) Map of the study area showing the Rocky Mountains in the State of Colorado (USA) and
904 the location of the Grand Junction meteorological station (GJT). The highlighted rectangular
905 area corresponds to the portion of the Rocky Mountains used as lower boundary condition
906 for the semi-idealized runs (but not to the simulation domain, which is somewhat larger).
907 (b) location of the turbulence reports possibly related to the atmospheric conditions present
908 on 7th February 2015 00 UTC, as described in Table 1, and surrounding landmarks. The
909 numbered aircraft symbols correspond to the turbulence reports ID in Table 1, the different
910 colors are: black for ModT, red for SevT, blue for ModMWT, pink for SevMWT. The map
911 only shows the portion of the Rocky Mountains used in the semi-idealized runs. Note that
912 the black outline is only used to delimit the figure, and does not correspond to the simulation
913 domain. 46

914 **Fig. 2.** Variation of the wind direction (a), wind speed (b) and the squared Brunt-Väisälä frequency
915 N^2 (d) with height for 7th February 2015 00 UTC. The meteorological data come from the
916 Grand Junction station, located upstream of the Rocky Mountains (station elevation: 1475
917 m) (see Fig.1). (c) shows again the variation of the wind direction with height, but uses
918 vectors with a constant length to represent the turning wind profile. Note that the vectors
919 point towards the vertical axis in the middle. 47

920 **Fig. 3.** 3D plots showing every point in the computational domain where $Ri_{out} \leq 0.25$ for the three
921 simulations performed with a real input sounding and a real orography (a), an idealized
922 mountain ridge (b), and a bell-shaped mountain (c) (Test 1). In (a) the Ri_{out} field contains
923 flow overturning regions where $Ri_{out} < 0$, and the simulation time shown is $t = 105$ min. In
924 (b) and (c) the simulation time shown is $t = 360$ min, however in (c) the Ri_{out} field is never
925 negative (at any simulation time). 48

926 **Fig. 4.** Horizontal cross-sections of the $Ri_{out} < 0$ field at $z \approx 7.5$ km, at the simulation time $t = 105$
927 min. (a) uses the real input sounding containing both speed and directional wind shear; (b)
928 uses the modified input sounding where only directional wind shear is present (Test 3). The
929 background field is the terrain elevation. 49

930 **Fig. 5.** Vertical (west-east) cross-sections at $Y = 180$ km in Fig.4 comparing the real sounding
931 simulation (a) with simulations run using a constant N (Test 2) (b), a constant wind direction
932 and a varying wind speed (Test 3) (c), a constant direction and wind speed (Test 4) using $U =$
933 10 m s^{-1} in (d) and $U = 20 \text{ m s}^{-1}$ in (e), at the simulation time $t = 180$ min. The background
934 field is the magnitude of the wave horizontal velocity perturbation vector (u', v') , the black
935 contours delimit $Ri_{out} < 0$ regions. 50

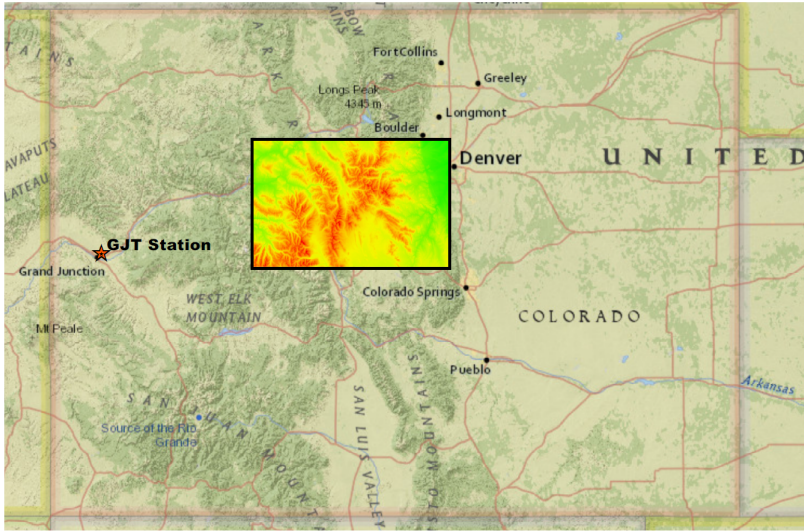
936 **Fig. 6.** Vertical (west-east) cross-sections of regions where $Ri_{out} < 0$ (a and c) and potential tem-
937 perature (b and d) fields passing through the point where turbulence was reported ($Y = 180$
938 km in Fig.4) at the simulation time $t = 135$ min. (a) and (b) correspond to the simulation
939 with the real input sounding. Figure (c) and (d) correspond to the simulation where speed
940 shear was neglected (Test 3). 51

941 **Fig. 7.** Horizontal cross-sections showing the flow transition as the degree of realism increases. The
942 background field is the magnitude of the (u', v') vector, the dashed contours mark the bottom
943 orography. In (b)-(e) the arrows are the background wind at the displayed level, the solid
944 contour lines are $Ri_{out} < 0$ (except for (c) where $0 < Ri_{out} \leq 0.25$). (a) analytical solution
945 from linear theory and (b) equivalent cross-section taken at $z \approx 7$ km for a simulation with
946 idealized orography and an idealized atmospheric sounding; (c) cross-section taken at $z \approx$
947 9.5 km for a simulation with idealized orography but a real atmospheric sounding (Test 1)

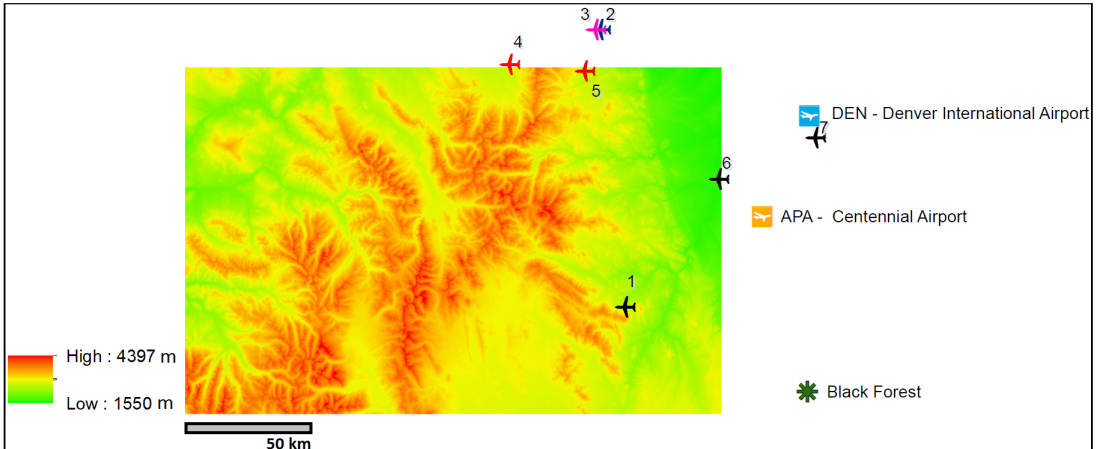
948 at $t = 360$ min; (d) as (c) but for a simulation with an idealized mountain ridge containing a
949 few peaks; (e) cross-section taken at $z \approx 7.5$ km for the semi-idealized simulation with real
950 orography and a real atmospheric sounding at $t = 105$ min. Note that (e) corresponds to a
951 portion of the simulation domain shown in Fig.4a, starting at $X = 240$ km, $Y = 110$ km. 52

952 **Fig. 8.** 2D power spectra of the horizontal velocity perturbation field for an idealized numerical
953 simulation of directional wind shear flow over an isolated axisymmetric mountain, computed
954 at heights of 3 km (a), 6.1 km (b), 7 km (c), 10 km (d), 13 km (e). The axes show the wave-
955 number components along x and y . The black arrows indicate the wind direction at each
956 height. 53

957 **Fig. 9.** 2D power spectra of the horizontal velocity perturbation field for the semi-idealized numeri-
958 cal simulation presented in section 4a, computed at heights corresponding to each kilometre
959 of the atmosphere between 5.5 and 15.5 km. Axes and black arrows as in Fig.8. 54

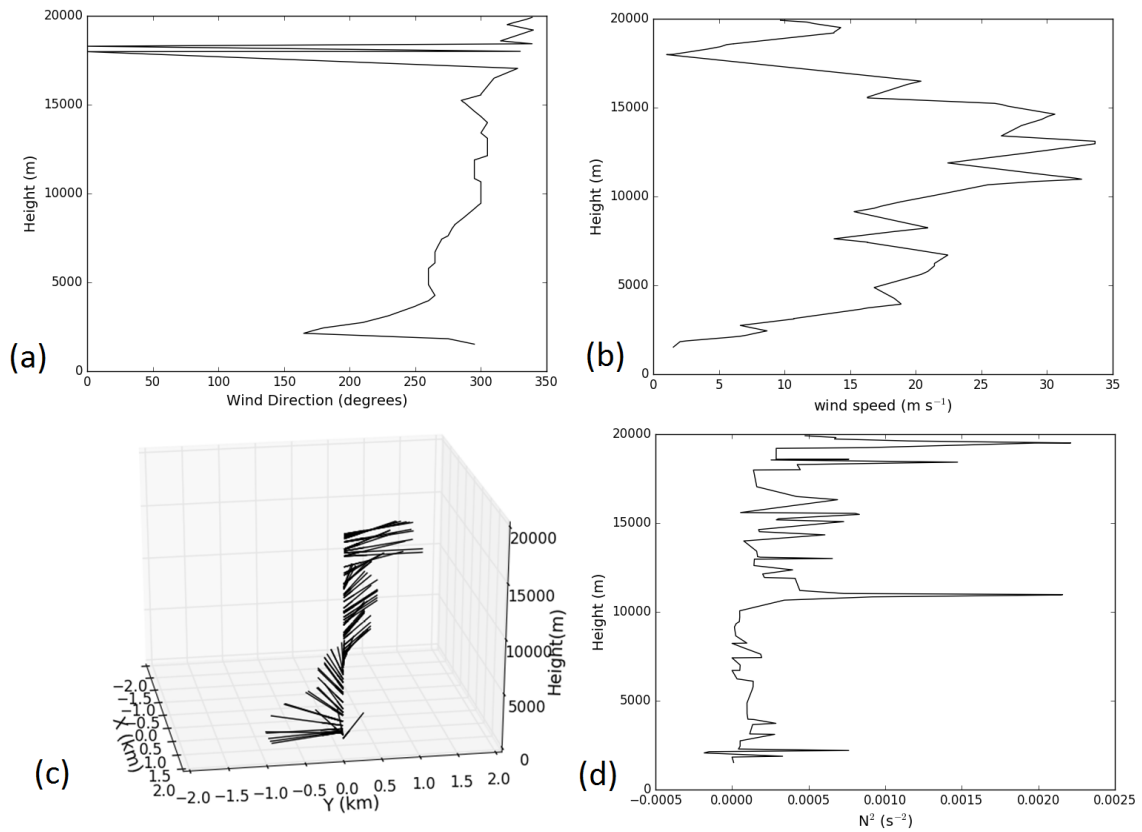


(a)

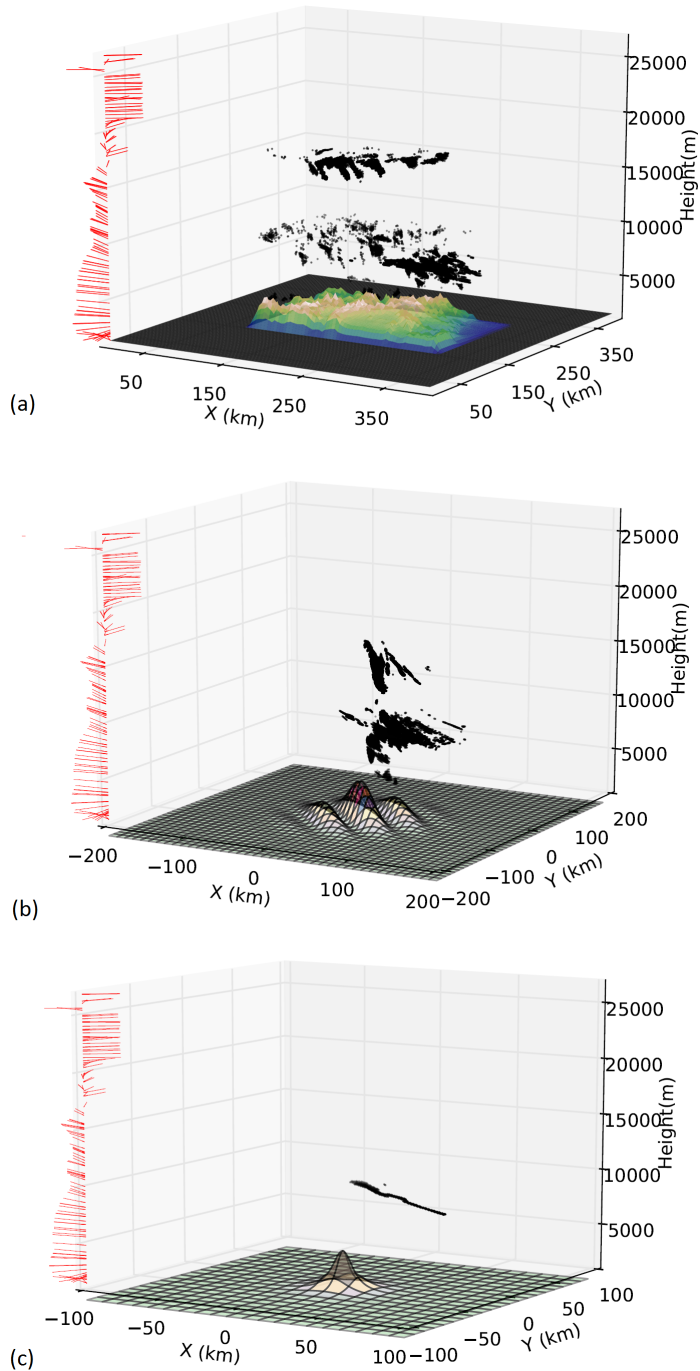


(b)

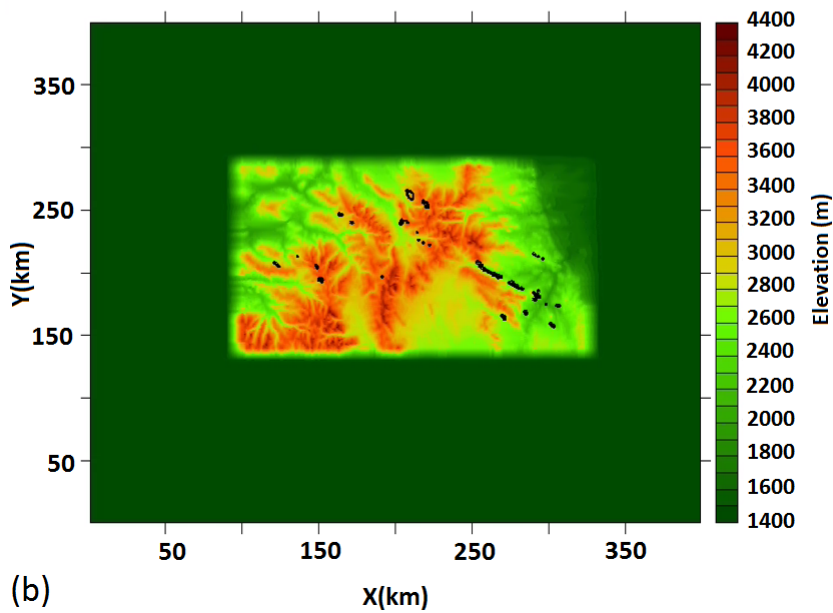
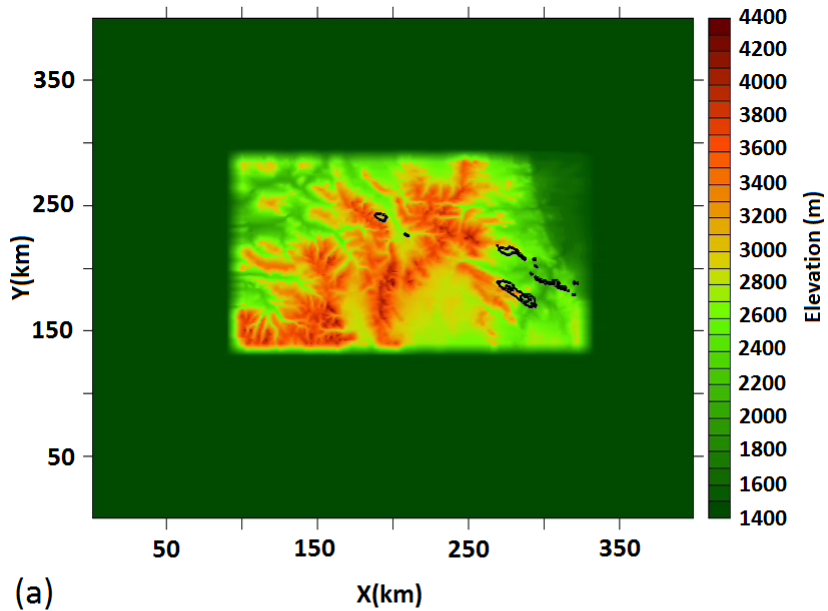
960 FIG. 1. (a) Map of the study area showing the Rocky Mountains in the State of Colorado (USA) and the
 961 location of the Grand Junction meteorological station (GJT). The highlighted rectangular area corresponds to
 962 the portion of the Rocky Mountains used as lower boundary condition for the semi-idealized runs (but not to
 963 the simulation domain, which is somewhat larger). (b) location of the turbulence reports possibly related to
 964 the atmospheric conditions present on 7th February 2015 00 UTC, as described in Table 1, and surrounding
 965 landmarks. The numbered aircraft symbols correspond to the turbulence reports ID in Table 1, the different
 966 colors are: black for ModT, red for SevT, blue for ModMWT, pink for SevMWT. The map only shows the
 967 portion of the Rocky Mountains used in the semi-idealized runs. Note that the black outline is only used to
 968 delimit the figure, and does not correspond to the simulation domain.



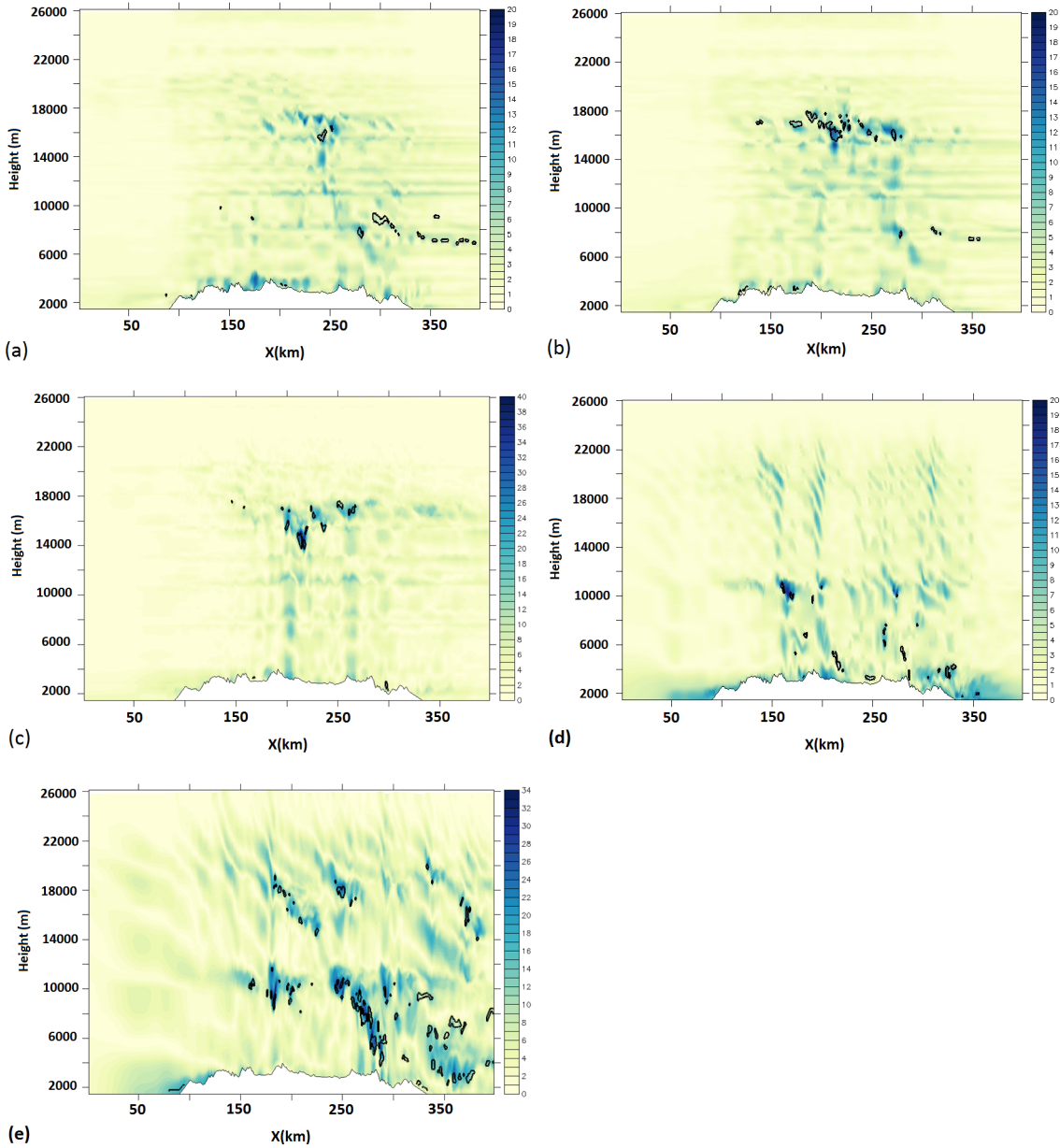
969 FIG. 2. Variation of the wind direction (a), wind speed (b) and the squared Brunt-Väisälä frequency N^2 (d)
 970 with height for 7th February 2015 00 UTC. The meteorological data come from the Grand Junction station,
 971 located upstream of the Rocky Mountains (station elevation: 1475 m) (see Fig.1). (c) shows again the variation
 972 of the wind direction with height, but uses vectors with a constant length to represent the turning wind profile.
 973 Note that the vectors point towards the vertical axis in the middle.



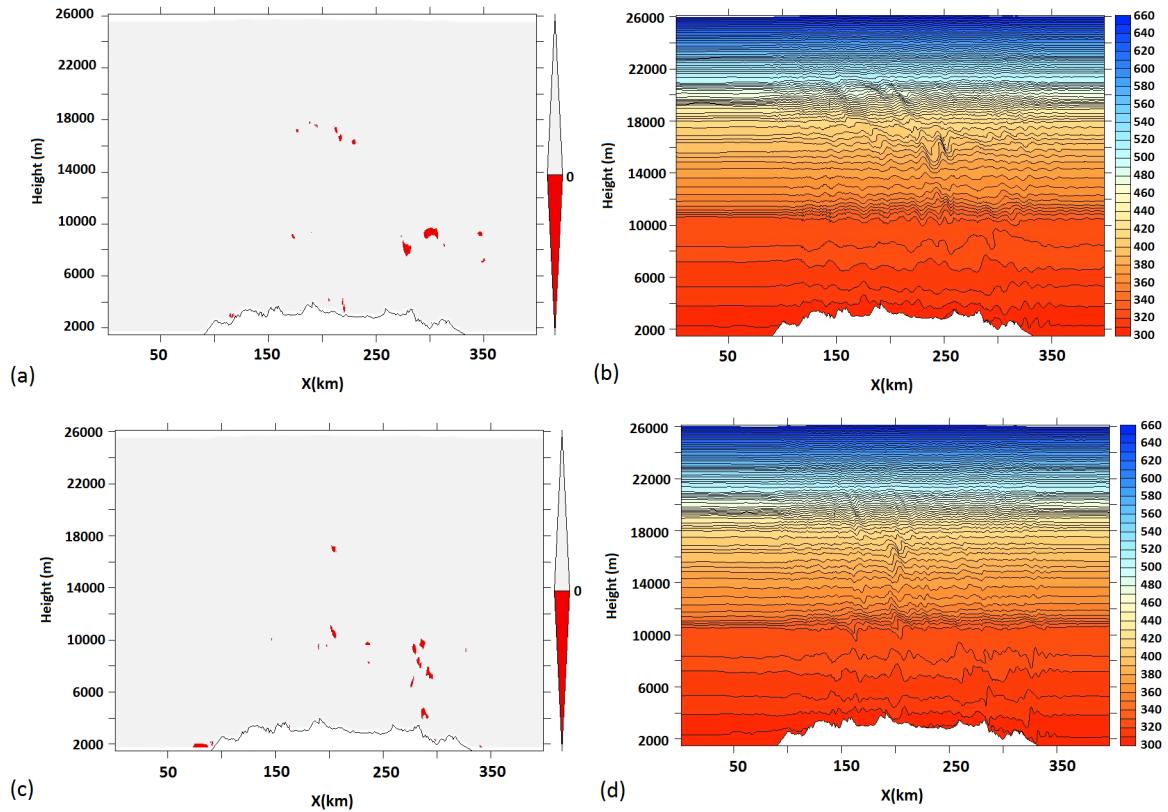
974 FIG. 3. 3D plots showing every point in the computational domain where $Ri_{out} \leq 0.25$ for the three simulations
 975 performed with a real input sounding and a real orography (a), an idealized mountain ridge (b), and a bell-shaped
 976 mountain (c) (Test 1). In (a) the Ri_{out} field contains flow overturning regions where $Ri_{out} < 0$, and the simulation
 977 time shown is $t = 105$ min. In (b) and (c) the simulation time shown is $t = 360$ min, however in (c) the Ri_{out} field
 978 is never negative (at any simulation time).



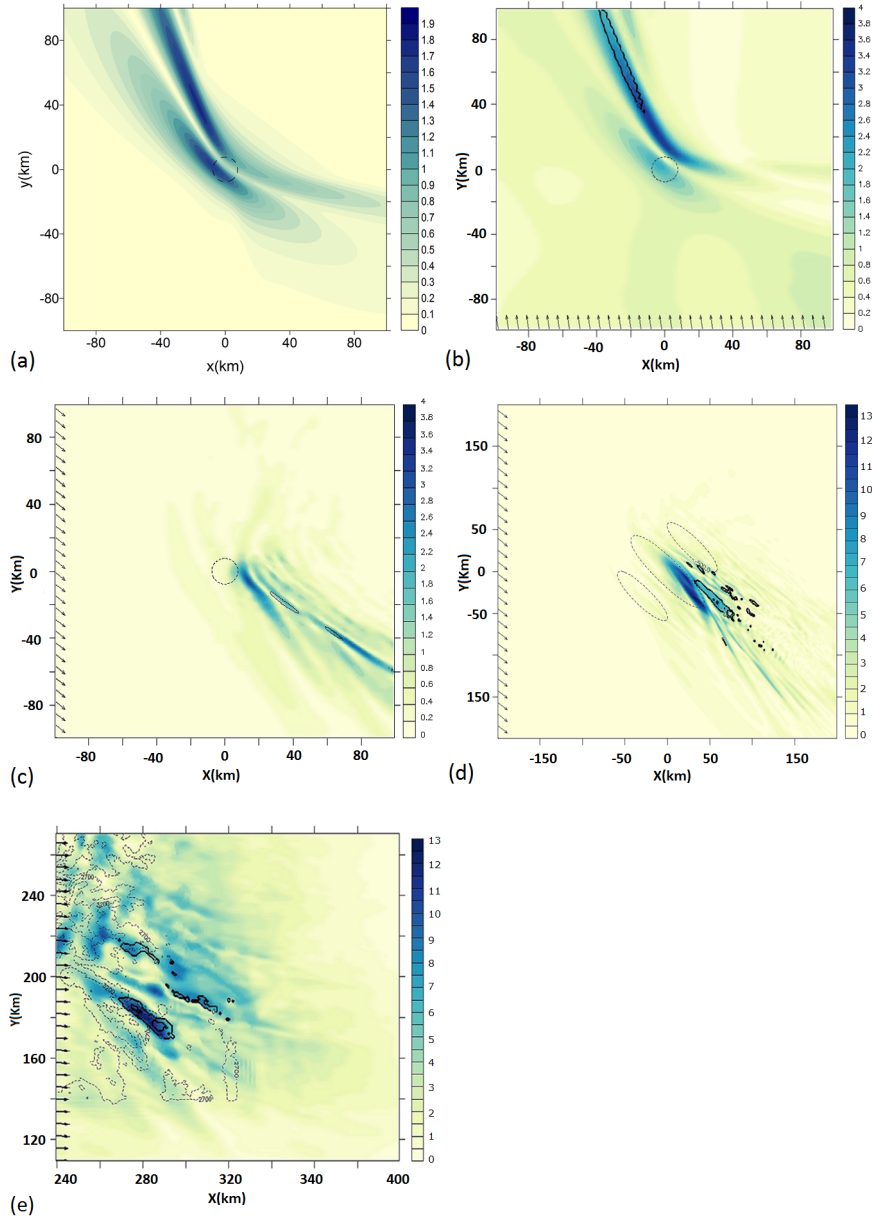
979 FIG. 4. Horizontal cross-sections of the $Ri_{out} < 0$ field at $z \approx 7.5$ km, at the simulation time $t = 105$ min.
 980 (a) uses the real input sounding containing both speed and directional wind shear; (b) uses the modified input
 981 sounding where only directional wind shear is present (Test 3). The background field is the terrain elevation.



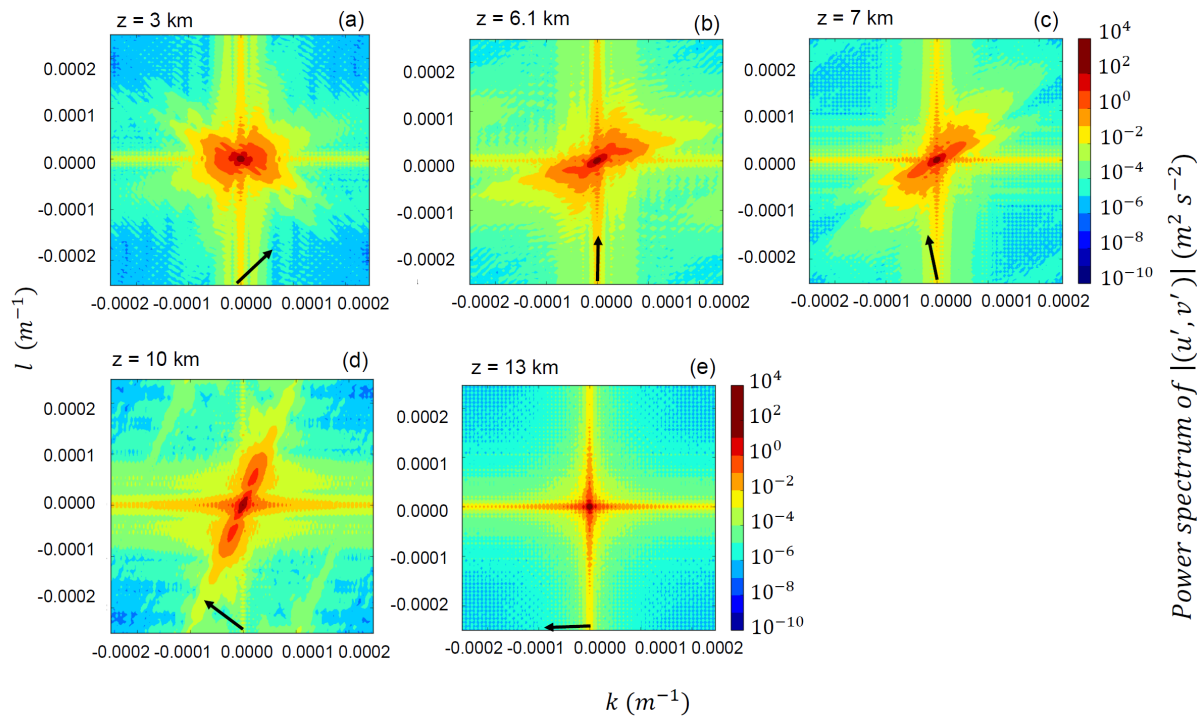
982 FIG. 5. Vertical (west-east) cross-sections at $Y = 180$ km in Fig.4 comparing the real sounding simulation (a)
 983 with simulations run using a constant N (Test 2) (b), a constant wind direction and a varying wind speed (Test
 984 3) (c), a constant direction and wind speed (Test 4) using $U = 10 \text{ m s}^{-1}$ in (d) and $U = 20 \text{ m s}^{-1}$ in (e), at the
 985 simulation time $t = 180$ min. The background field is the magnitude of the wave horizontal velocity perturbation
 986 vector (u', v') , the black contours delimit $Ri_{out} < 0$ regions.



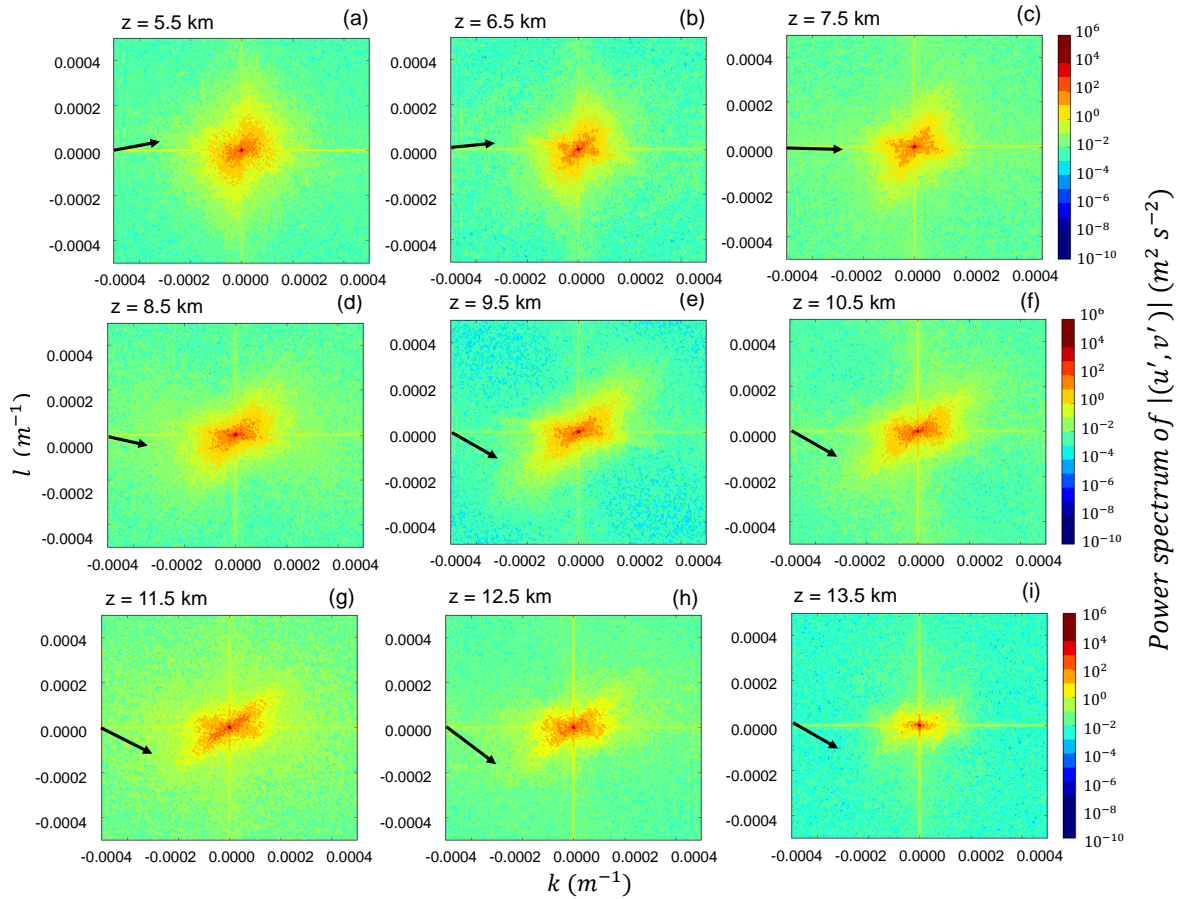
987 FIG. 6. Vertical (west-east) cross-sections of regions where $Ri_{out} < 0$ (a and c) and potential temperature (b
 988 and d) fields passing through the point where turbulence was reported ($Y = 180$ km in Fig.4) at the simulation
 989 time $t = 135$ min. (a) and (b) correspond to the simulation with the real input sounding. Figure (c) and (d)
 990 correspond to the simulation where speed shear was neglected (Test 3).



991 FIG. 7. Horizontal cross-sections showing the flow transition as the degree of realism increases. The back-
 992 ground field is the magnitude of the (u', v') vector, the dashed contours mark the bottom orography. In (b)-(e)
 993 the arrows are the background wind at the displayed level, the solid contour lines are $Ri_{out} < 0$ (except for (c)
 994 where $0 < Ri_{out} \leq 0.25$). (a) analytical solution from linear theory and (b) equivalent cross-section taken at $z \approx$
 995 7 km for a simulation with idealized orography and an idealized atmospheric sounding; (c) cross-section taken
 996 at $z \approx 9.5$ km for a simulation with idealized orography but a real atmospheric sounding (Test 1) at $t = 360$ min;
 997 (d) as (c) but for a simulation with an idealized mountain ridge containing a few peaks; (e) cross-section taken
 998 at $z \approx 7.5$ km for the semi-idealized simulation with real orography and a real atmospheric sounding at $t = 105$
 999 min. Note that (e) corresponds to a portion of the simulation domain shown in Fig.4a, starting at $X = 240$ km, Y
 1000 = 110 km.



1001 FIG. 8. 2D power spectra of the horizontal velocity perturbation field for an idealized numerical simulation
 1002 of directional wind shear flow over an isolated axisymmetric mountain, computed at heights of 3 km (a), 6.1 km
 1003 (b), 7 km (c), 10 km (d), 13 km (e). The axes show the wave-number components along x and y . The black
 1004 arrows indicate the wind direction at each height.



1005 FIG. 9. 2D power spectra of the horizontal velocity perturbation field for the semi-idealized numerical simu-
 1006 lation presented in section 4a, computed at heights corresponding to each kilometre of the atmosphere between
 1007 5.5 and 15.5 km. Axes and black arrows as in Fig.8.